Convective Systems over the South China Sea: Cloud-Resolving Model Simulations

W.-K. TAO

Laboratory for Atmospheres, NASA Goddard Space Flight Center, Greenbelt, Maryland

C.-L. SHIE

Laboratory for Atmospheres, NASA Goddard Space Flight Center, Greenbelt, and Goddard Earth Sciences and Technology Center, University of Maryland, Baltimore County, Baltimore, Maryland

J. SIMPSON AND S. BRAUN

Laboratory for Atmospheres, NASA Goddard Space Flight Center, Greenbelt, Maryland

R. H. JOHNSON AND P. E. CIESIELSKI

Department of Atmospheric Science, Colorado State University, Fort Collins, Colorado

(Manuscript received 31 July 2002, in final form 28 May 2003)

ABSTRACT

The two-dimensional version of the Goddard Cumulus Ensemble (GCE) model is used to simulate two South China Sea Monsoon Experiment (SCSMEX) convective periods [18–26 May (prior to and during the monsoon onset) and 2–11 June (after the onset of the monsoon) 1998]. Observed large-scale advective tendencies for potential temperature, water vapor mixing ratio, and horizontal momentum are used as the main forcing in governing the GCE model in a semiprognostic manner. The June SCSMEX case has stronger forcing in both temperature and water vapor, stronger low-level vertical shear of the horizontal wind, and larger convective available potential energy (CAPE).

The temporal variation of the model-simulated rainfall, time- and domain-averaged heating, and moisture budgets compares well to those diagnostically determined from soundings. However, the model results have a higher temporal variability. The model underestimates the rainfall by 17% to 20% compared to that based on soundings. The GCE model-simulated rainfall for June is in very good agreement with the Tropical Rainfall Measuring Mission (TRMM), precipitation radar (PR), and the Global Precipitation Climatology Project (GPCP). Overall, the model agrees better with observations for the June case rather than the May case.

The model-simulated energy budgets indicate that the two largest terms for both cases are net condensation (heating/drying) and imposed large-scale forcing (cooling/moistening). These two terms are opposite in sign, however. The model results also show that there are more latent heat fluxes for the May case. However, more rainfall is simulated for the June case. Net radiation (solar heating and longwave cooling) are about 34% and 25%, respectively, of the net condensation (condensation minus evaporation) for the May and June cases. Sensible heat fluxes do not contribute to rainfall in either of the SCSMEX cases. Two types of organized convective systems, unicell (May case) and multicell (June case), are simulated by the model. They are determined by the observed mean U wind shear (unidirectional versus reverse shear profiles above midlevels).

Several sensitivity tests are performed to examine the impact of the radiation, microphysics, and large-scale mean horizontal wind on the organization and intensity of the SCSMEX convective systems.

1. Introduction

The global hydrological cycle is central to the earth's climate system. Rainfall and its associated precipitation processes are a key link in the hydrological cycle. Freshwater provided by tropical rainfall and its variability can exert a large impact upon the structure and motions of the upper-ocean layer. In addition, two-thirds of the global rain falls in the Tropics, while the associated latent heat release accounts for three-fourths of the total heat energy for the earth's atmosphere. The Tropical Rainfall Measuring Mission (TRMM), a joint United States–Japan project, is a satellite mission intended to provide an adequate measurement of rainfall, as well as an estimation of the four-dimensional structure of diabatic heating over the global Tropics (Simpson et al. 1988). The distributions of rainfall and inferred heating

Corresponding author address: Dr. Wei-Kuo Tao, Mesoscale Atmospheric Processes Branch, Code 912, NASA GSFC, Greenbelt, MD 20771.
E-mail: tao@agnes.gsfc.nasa.gov

© 2003 American Meteorological Society

can be used to advance our understanding of the global energy and water cycle, as well as for global circulation and climate models for testing and improving their parameterizations.

Cloud-resolving (or cumulus ensemble) models (CRMs) are one of the most important tools to establish quantitative relationships between diabatic heating and rainfall. This is because latent heating is dominated by phase changes between water vapor and small, cloud-sized particles, which cannot be directly detected. The CRMs, however, explicitly simulate the conversion of cloud condensate into raindrops and various forms of precipitation ice. These different forms of precipitation are most readily detected from space, and ultimately reach the surface in the form of rain. The Goddard Cumulus Ensemble (GCE) model is a CRM and has been used to provide cloud datasets associated with various types of clouds/cloud systems from different geographic locations for improving the performance of the TRMM retrieval algorithms (see a review by Simpson et al. 1996).

Several field campaigns conducted during 1998 and 1999 were aimed at the validation of TRMM products (i.e., rainfall and the vertical distribution of latent heating). Because latent heating profiles cannot be directly measured, CRMs are used in TRMM algorithms to provide a link between the latent heating profiles, TRMM precipitation radar (PR), and microwave radiometer imager (TMI) observations. Consequently, one of the key components of the TRMM field campaigns is to provide observations of the structure and evolution of mesoscale convective systems (MCSs), individual convective clouds, and their embedded large-scale environment. CRMs require these datasets for initial conditions as well as for the validation of their vertical latent heating structure. The South China Sea Monsoon Experiment (SCSMEX) was one of four major TRMM field campaigns and was conducted in May–June 1998. One of its major objectives is to better understand the key physical processes for the onset and evolution of the summer monsoon over Southeast Asia and southern China (Lau et al. 2000). Multiple observation platforms (e.g., upper-air soundings, Doppler radar, ships, wind profilers, radiometers, etc.) during SCSMEX provided a first attempt at investigating the detailed characteristics of convection and circulation changes associated with monsoons over the South China Sea region. SCSMEX also provided precipitation derived from atmospheric sounding budgets (Johnson and Ciesielski 2002) and dual Doppler radar (Wang 2003, manuscript submitted to *Mon. Wea. Rev.*).

The use of CRMs in the study of tropical convection and its relation to the large-scale environment can be generally categorized into two methodologies. The first approach is so-called cloud ensemble modeling. In this approach, many clouds/cloud systems of different sizes in various stages of their life cycles can be present at any model simulation time. The large-scale effects that are derived from observations are imposed into the models as the main forcing, however. In addition, the cloud ensemble models use cyclic lateral boundary conditions (to avoid reflection of gravity waves) and require a large horizontal domain (to allow for the existence of an ensemble of clouds). The advantage of this approach is that the modeled convection will be forced to almost the same (but not identical) intensity, thermodynamic budget, and organization as the observations. This approach will also allow the cloud-resolving model to perform multiday or multiweek time integration. On the other hand, the second approach for cloud-resolving models usually requires initial temperature and water vapor profiles that have a medium to large convective available potential energy (CAPE), and an open lateral boundary condition is used. The modeled clouds, then, are initialized with either a cool pool, warm bubble, or surface processes (i.e., land/ocean fluxes). The key developments in the cloud ensemble modeling using the large-scale forced convection approach over the past two decades were discussed in Johnson et al. (2002) and Tao (2003).

In this paper, the GCE model will be used to perform two multiday integrations using SCSMEX data following the first approach. The first one is prior to and during the monsoon onset period, and the second is after the onset of the monsoon. The objectives of this modeling paper are 1) to examine the characteristics of surface rainfall in the convective and stratiform regions, 2) to calculate and examine the vertical distribution of the latent heating and its structure in the convective and stratiform regions, 3) to examine the microphysical processes (condensation/evaporation, deposition/sublimation, and melting/freezing), and 4) to compute and analyze the thermodynamic budgets (domain-averaged budget). The similarities and differences prior to, during, and after the onset of the monsoon will be discussed. In addition, the impact of microphysical processes, radiation, and the vertical shear of the horizontal wind on model results will be examined through sensitivity tests.

2. Large-scale environmental conditions

Johnson and Ciesielski (2002) calculated the apparent heat source (Q_1) and apparent moisture sink (Q_2), which can be used to validate TRMM rainfall products. In addition, the horizontal and vertical advective components in Q_1 and Q_2 can be used as large-scale advective forcing for the CRMs (Soong and Tao 1980; Moncrieff et al. 1997). Two major convective events around 18–26 May and 2–11 June 1998 were identified and selected for model simulation. The first event is prior to and during the onset of the monsoon; the second is post-onset. Figure 1 shows the time series of large-scale advective forcing in temperature and water vapor associated with these two SCSMEX events that were used for the GCE model simulations. Both cases show a sim-

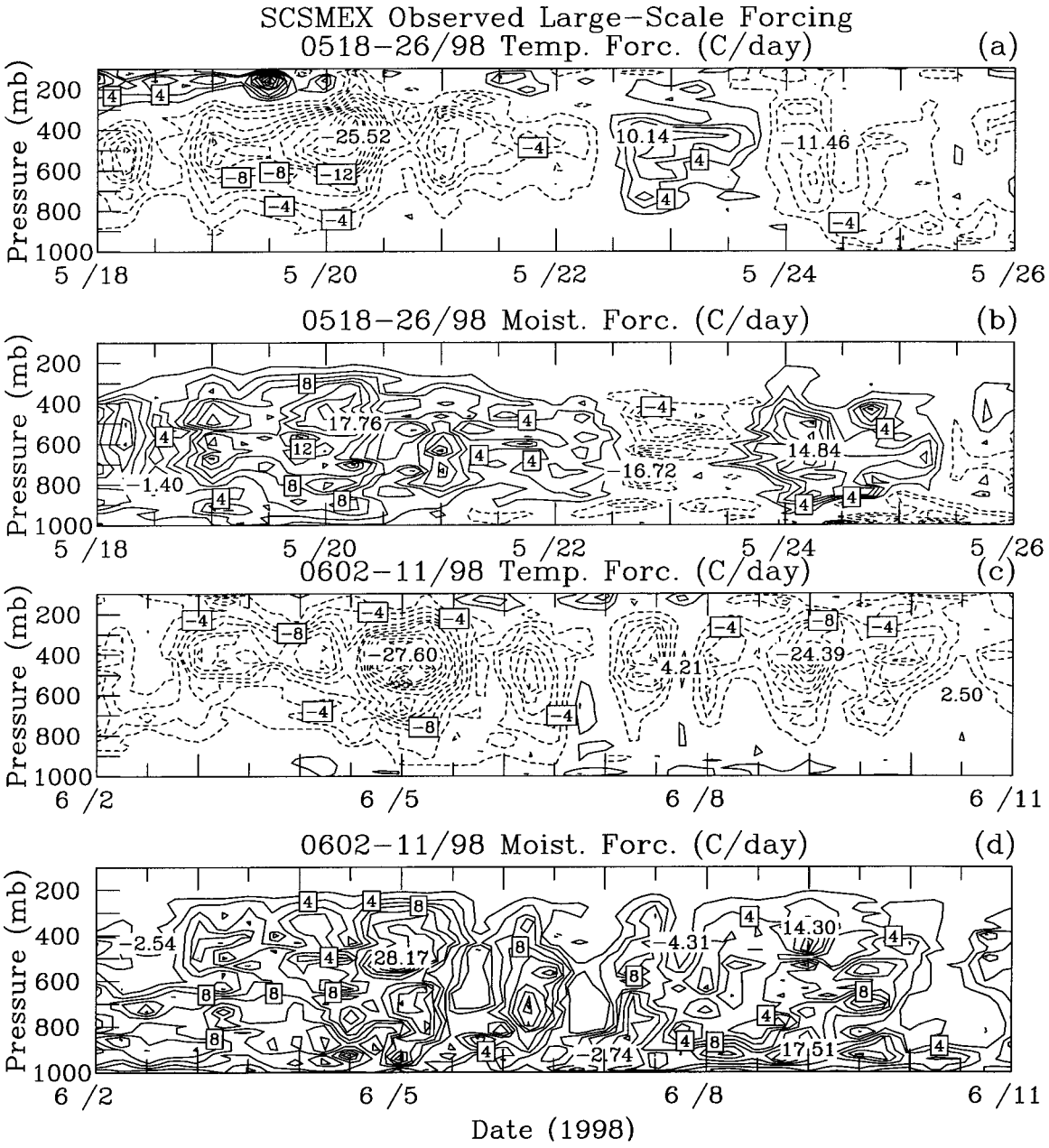

FIG. 1. Horizontally averaged diagnosed large-scale advective forcing in (a) temperature (°C day^{-1}) and (b) water vapor (°C day^{-1}) for the 18–26 May 1998 period. (c), (d) Same as (a) and (b), except for the 2–11 Jun 1998 period. The contour interval is 2°C day^{-1}. Note that positive (negative) indicates moistening (drying) in (b) and (d).

ilar order of magnitude of peak heating, 22–26°C day^{-1} between 350 and 500 mb. However, the mean large-scale forcing associated with these two cases is quite different (Fig. 2). The June case has stronger forcing in both temperature and water vapor. In addition, the temperature forcing is located higher in the June case compared to the May case. The large-scale forcing in water vapor is much stronger in the lower and middle troposhere in the June case. Also, the large-scale forcing in water vapor has more complex vertical structures (multipeaks) in SCSMEX compared to those of the Global Atmospheric Research Program (GARP) Atlantic Experiment (GATE) and the Tropical Ocean Global Atmosphere Coupled Ocean–Atmosphere Response Experiment (TOGA COARE; single peaks located at low to middle altitude).

The observed time series of mean zonal, meridional, and vertical wind are shown in Figs. 3 and 4, respectively. Differences between these two periods are quite significant. There is stronger low-level vertical shear in

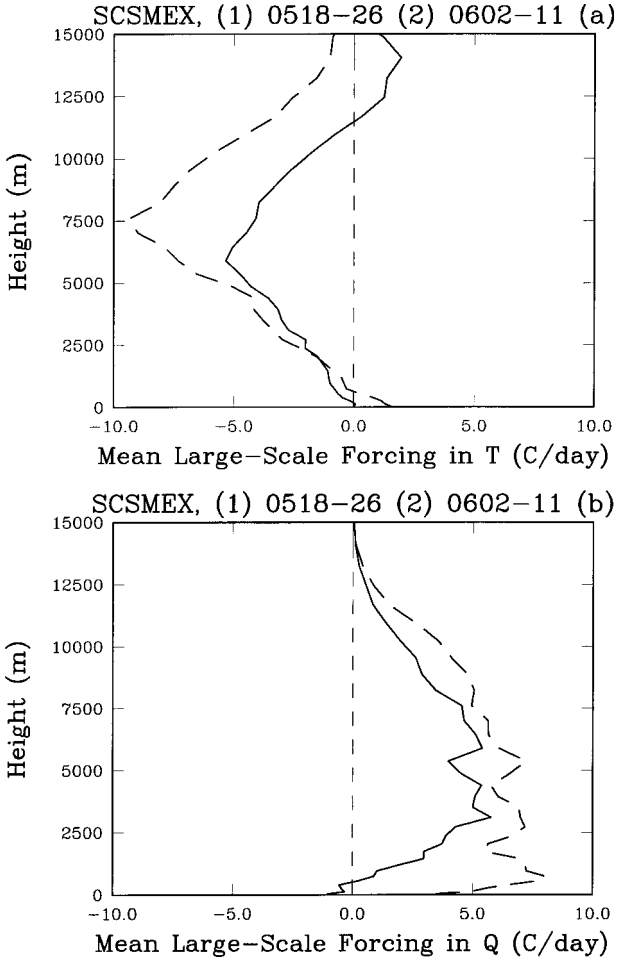

FIG. 2. Time-averaged large-scale advective forcing in (a) temperature °C day^{-1} and (b) water vapor °C day^{-1}. The solid line is the 18–26 May 1998 period, and the dashed line the 2–11 Jun 1998 period.

the *u* wind component during the June period. The mean vertical velocity is stronger and at a higher altitude in June. This feature is consistent with the large-scale advective forcing in temperature and water vapor because the vertical advection term in the Q_1 and Q_2 budgets is always much larger than its horizontal counterpart for deep convective events in the Tropics (i.e., Soong and Tao 1980). The *u* wind component is quite different between an active convective period (i.e., 18–22 May) and inactive one (22–24 May). The wind changed from westerly to easterly at the lower and upper troposphere around 22 May. There are about six and eight to nine major convective events, respectively, shown in the large-scale advective forcing in temperature and water vapor, and large-scale mean vertical velocity for the May and June cases.

Table 1 compares several characteristics of the large-scale flow (stability, lifted index, precipitable water, and Richardson number) in which these two SCSMEX systems were embedded. The vertically integrated water vapor contents are quite moist (62.58 and 62.34 g cm^{-2}, respectively) for both cases. A very moist environment in the Pacific region [Winter Monsoon Experiment (WMONEX), Australian Monsoon Experiment (AMEX), and Equatorial Mesoscale Experiment (EMEX)] is quite a common feature. The bulk Richardson number is larger in the June case because of the stronger instability. The CAPE and lifted index are also larger in the June period than in the May one.

3. The Goddard Cumulus Ensemble model and model setups

a. The GCE model

The model used in this study is the two-dimensional (2D) version of the Goddard Cumulus Ensemble model. The equations that govern cloud-scale motion (wind) are anelastic by filtering out sound waves. The subgrid-scale turbulence used in the GCE model is based on work by Klemp and Wilhelmson (1978). In their approach, one prognostic equation is solved for subgrid kinetic energy, which is then used to specify the eddy coefficients. The effect of condensation on the generation of subgrid-scale kinetic energy is also incorporated in the model (see Soong and Ogura 1980). The cloud microphysics include a parameterized two-category liquid water scheme (cloud water and rain), and a parameterized Lin et al. (1983) or Rutledge and Hobbs (1984) three-category ice-phase scheme (cloud ice, snow, and hail/graupel). Solar and infrared radiation parameterizations are also included in the model (Tao et al. 1996). The TOGA COARE bulk flux algorithm (Fairall et al. 1996) is used for calculating the surface fluxes (Wang et al. 1996). All scalar variables use forward time differencing and a positive definite advection scheme with a nonoscillatory option (Smolarkiewicz and Grabowski 1990). The dynamic variables use a second-order accurate advection scheme and a leapfrog time integration (kinetic energy semiconserving method). Details of the GCE model description can be found in Tao and Simpson (1993) and Tao et al. (2003).

For the present study, a stretched vertical coordinate with 41 levels is used. The model has finer resolution (about 80 m) in the boundary layer and coarser resolution (about 1000 m) in the upper levels. The grid spacing in the horizontal plane is 1000 m with 512 grid points. The time step is 7.5 s. Surface fluxes from the ocean and cloud–radiation interactive processes are explicitly included. The observed sea surface temperature (SST) was used for latent and sensible heat flux calculations.

b. Model setup for imposing the large-scale advective forcing

Observed large-scale advective tendencies (or forcing) of potential temperature, water vapor mixing ratio,

and horizontal momentum (Figs. 1 and 3) are used as the main large-scale forcing in governing the GCE model in a semiprognostic manner. The large-scale advective tendencies for potential temperature and water vapor mixing ratio,

$$\left(\frac{\partial\overline{\theta}}{\partial t}\right)_{\text{L.S.}} = -\overline{\mathbf{v}}\cdot\nabla\overline{\theta} - \overline{w}\frac{\partial\overline{\theta}}{\partial z} \quad \text{and}$$

$$\left(\frac{\partial\overline{q}}{\partial t}\right)_{\text{L.S.}} = -\overline{\mathbf{v}}\cdot\nabla\overline{q} - \overline{w}\frac{\partial\overline{q}}{\partial z},$$

were derived every 6 h over the SCSMEX analyses. Because accurate calculations of the large-scale horizontal momentum forcing terms are difficult to obtain from observations in the Tropics, these terms were instead replaced by a nudging term:

$$\left(\frac{\partial\overline{\mathbf{v}}}{\partial t}\right)_{\text{L.S.}} = \frac{\overline{\mathbf{v}} - \overline{\mathbf{v}}_{\text{obs}}}{\tau},$$

where $\overline{\mathbf{v}}$ is the model domain-averaged horizontal velocity, $\overline{\mathbf{v}}_{\text{obs}}$ is the observed large-scale horizontal velocity, and τ is the specified adjustment time scale (1 h). This method constrains the domain-averaged horizontal velocities to follow the observed values and thereby provides a simple means to controlling the cloud system dynamics by the large-scale momentum and shear. Cyclic lateral boundary conditions were incorporated to ensure that there was no additional heat, moisture, or momentum forcing inside the domain apart from the large-scale forcing (Soong and Tao 1980; Tao and Soong 1986). This type of cloud-resolving modeling was used by many recent modeling studies for studying GATE and TOGA COARE convective systems (Grabowski et al. 1998; Xu and Randall 1996; Wu et al. 1998; Donner et al. 1999; Petch and Gray 2001; Johnson et al. 2002).

c. Convective–stratiform partitioning method

In the GCE model convective–stratiform partitioning method, convective, stratiform, and nonsurface precipitation regions are identified using the information from surface rain rates first (Churchill and Houze 1984). Two additional criteria are applied, which have been included to identify regions where convection may be quite active *aloft* though there is little or no precipitation yet at the surface, such as areas associated with tilted updrafts and *new cells* initiated ahead of an organized squall line (Tao and Simpson 1989; Tao et al. 1993). Nonsurface precipitation regions are considered to be convective if cloud water exceeds a certain threshold (i.e., 0.5 g kg^{-1}), or if the updraft exceeds a certain threshold (i.e., 3 m s^{-1}) below the melting level. The presence of this amount of cloud water is a good indication of a saturated area (100% relative humidity). Chin (1994), W. R. Cotton (1998, personal communication), and Redelsperger et al. (2000) have adopted this method. Different convective and stratiform separation techniques (Churchill and Houze 1984; Tao et al. 1993; Xu 1995; Caniaux et al. 1994; and Steiner et al. 1995) were examined and compared by Lang et al. (2003).

4. Results

a. Surface rainfall characteristics

Figures 5a and 5b show the time series of the GCE model-simulated surface rain rate for two SCSMEX convective periods, 18–26 May (prior to and during the monsoon) and 2–11 June (after the onset of the monsoon) 1998. Ensembles of clouds and cloud systems with various sizes are simulated by the model and they propagate from west to east in both cases. However, the convective systems in the May case propagated slower than those in the June case. In addition, cloud–cloud interactions and merging[1] are a more common feature for the May period. Some of the convection simulated in the May case exhibits characteristics that are quite similar to those of unicell convection[2] (Figs. 6e–6h). The mean *U* wind shear in the May SCSMEX case (Fig. 4a) does not reverse sign above midlevels (3–5-km level) as it does for the June case. With a unidirectional shear profile of the *U* wind, the model simulates unicell-type convection (Dudhia et al. 1987; Tao et al. 1995). On the other hand, the model can produce multicell type convection with the reversing shear profile in the June case (Figs. 6a–6d). In general, these types of convective systems can contribute significant amounts of surface rainfall and associated latent heating. The simulated cloud system in the June case reproduces qualitatively several important features typically associated with tropical squall systems (Houze 1977; Zipser 1977). For example, narrow convective cores are located at the leading edge of the system with a widespread trailing stratiform region. The upshear tilt of the core updrafts and a rear inflow extending from the middle troposphere to the leading edge of the cool pool are well simulated. In addition, a strong cold pool associated with a squall mesohigh and a wake low are also present in the simulation. For the unicell type of convection, it has characteristics of a single updraft, much less stratiform cloud coverage, and a mesoscale circulation that is weaker than in the squall type of convection. The cool pool is much weaker and less organized than in the organized type of convection.

Figure 7 shows time series of rainfall rates averaged over the SCSMEX region that were simulated by the GCE model and estimated from soundings. The temporal variation of the GCE model–simulated rainfall is in very good agreement with that estimated from water

[1] The modeled merger is a first-order merger as defined in Simpson et al. (1980) that is the result of the joining of two or more previously independent single clouds.

[2] Many unicell type convective systems were definitely observed in May (Wang 2003).

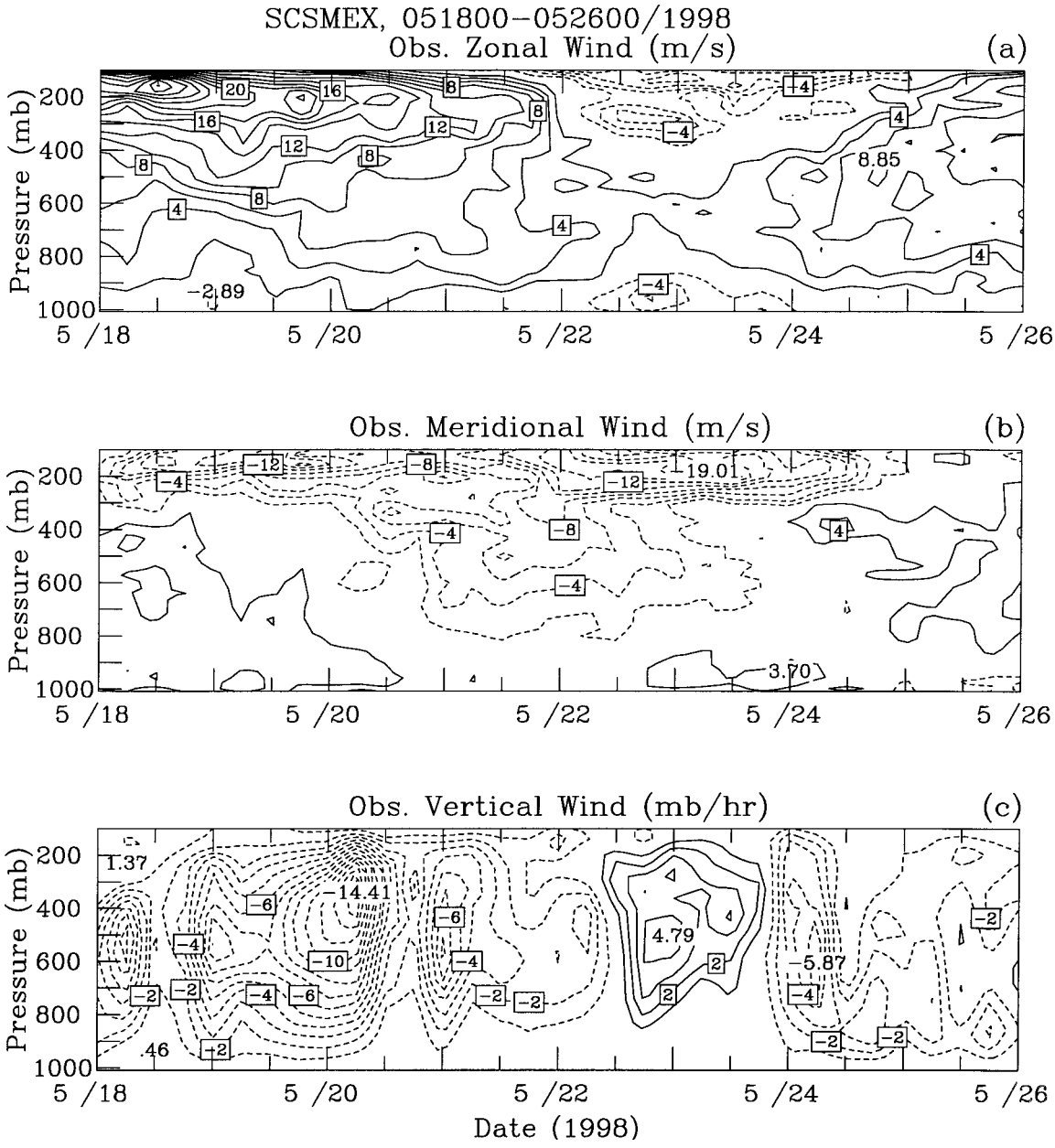

FIG. 3. Horizontally averaged mean large-scale (a) u wind (m s^{-1}), (b) v wind (m s^{-1}), and (c) w velocity (mb h^{-1}) for the 18–26 May 1998 period. The contour interval is 2 m s^{-1}, 2 m s^{-1}, and 1 mb h^{-1} for (a), (b), and (c), respectively. (d), (e), (f) Same as (a), (b), and (c), except for the 2–11 Jun 1998 period.

vapor budget determined from soundings (Johnson and Ciesielski 2002). The good agreement is caused by the fact that the GCE model was forced by large-scale tendencies in temperature and water vapor computed from the sounding network. When the imposed large-scale advective forcing cools and moistens the environment, the model responds by producing clouds through condensation and deposition. The fallout of large precipitation particles produces rainfall at the surface. The larger the advective forcing, the larger the microphysical response (rainfall) the model will produce (Soong and Tao 1980; Tao and Simpson 1984). On the other hand, the model will not produce any cloud or rainfall when the imposed large-scale advective forcing heats and dries the atmosphere (i.e., no rainfall before and during 23 May).

Rainfall probability distribution, both simulated and estimated by soundings, for these two SCSMEX cases are shown in Fig. 8. In the May case, a bimodal distribution is estimated by the sounding, but not simulated by the model. In contrast, there is only a single peak for both simulated and observed distributions for the

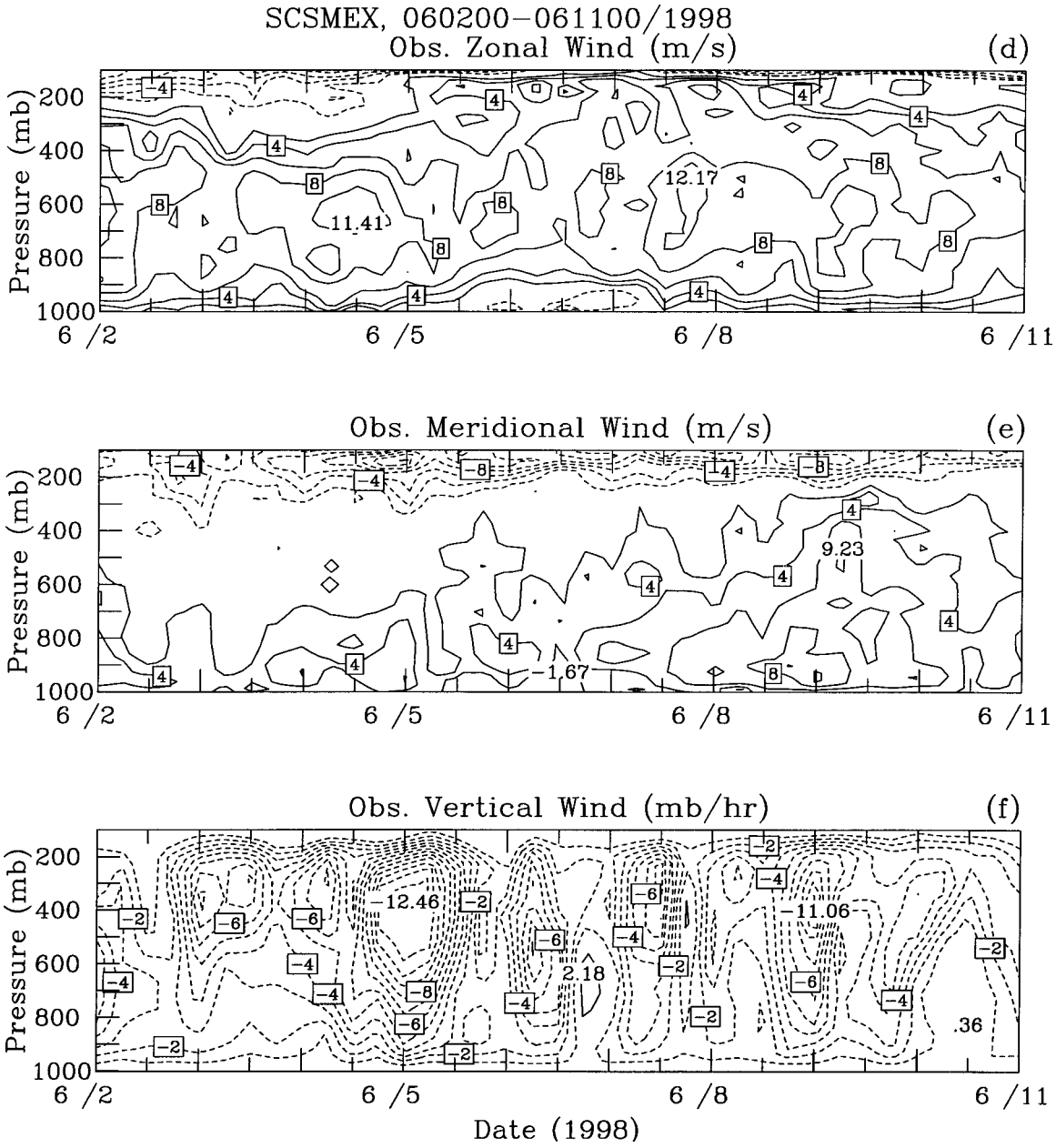

FIG. 3. (*Continued*)

June case. The GCE model results also indicate that there is more light rain (less than 1 mm h^{-1}), both simulated and observed in May case. The weaker large-scale advective forcing in May produced more light rainfall. In addition, the weaker shear profile (*U* wind) in the lower troposphere (Fig. 4a) can aid in producing more light rain in May.

The rainfall amounts from the GCE model, soundings, the TRMM PR, TMI, and Global Precipitation Climatology Project (GPCP) are shown in Table 2. They all indicate that less rainfall occurs in the May case than in the June case. Surprisingly, the model underestimated rainfall by 17% and 20%, respectively, for the May and June cases compared to that calculated based on soundings. It is unclear why the model underestimated rainfall even though the GCE model was forced by large-scale tendencies in temperature and water vapor computed from the sounding network. Two additional sources of forcing, ocean surface fluxes and radiation, could be underestimated by the model. The model physics may be another reason for this discrepancy. Accurate and consistent large-scale advective tendencies in temperature and water vapor are also needed for CRM simulation. Tao et al. (2000) found

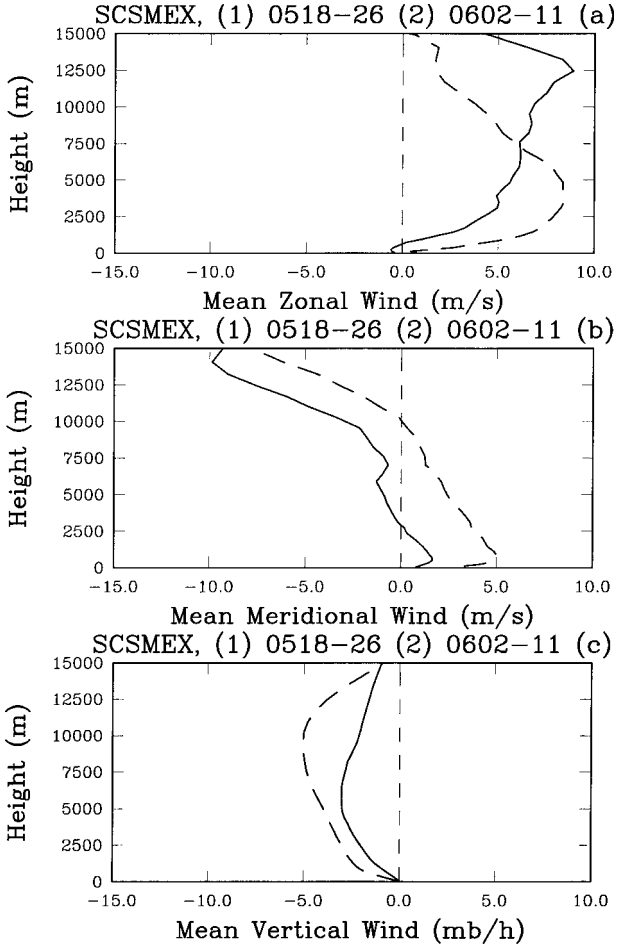

FIG. 4. Time-averaged large-scale (a) *u*, (b) *v*, and (c) *w* wind components. The solid line is for the 18–26 May 1998 period, and dashed line is for the 2–11 Jun 1998 period.

that the large-scale advective terms for temperature and water vapor are not always consistent. For example, large-scale forcing could indicate strong drying (which would produce cooling in the model through evaporation) but could not contain large-scale advective heating to compensate. This discrepancy in forcing would cause differences between the observed and modeled rainfall.

The smaller large-scale advective forcing in temperature and water vapor, and the *U* wind shear profile for the May case produce more light precipitation that is categorized as stratiform than those in the June case (see Fig. 8). That is why more stratiform rain is simulated in the May case than the June case (Table 2). There is a relatively small difference (less than 7%) in stratiform percentage between the model and TRMM (both PR and TMI) for the June case compared to the May case (over 16%). The GCE model–simulated rainfall for June is also in very good agreement with the TRMM PR and GPCP. However, comparisons between the GCE model results (using 1-km grid size) and satellite data should be made with caution because of the resolution difference and sampling issues.

TABLE 1. Initial environmental conditions expressed in terms of CAPE, lifted index, precipitable water, and Richardson number for the 18–26 May and 2–11 Jun 1998 periods. The lifted index is defined as the difference in °C between the temperature at 500 mb and the temperature of a parcel averaged over the lowest 100 mb and lifted to 500 mb.

	CAPE (m^2 s^{-2})	Lifted index	Precipitable water (g cm^{-2})	Richardson number
18–26 May 1998	825	−0.91	62.53	55.4
2–11 Jun 1998	1324	−1.92	62.34	100.28

b. Vertical distribution of Q_1 and Q_2 budget

In diagnostic studies (e.g., Yanai et al. 1973), it is customary to define the apparent heat source Q_1 and the apparent moisture sink Q_2 of a large-scale system by averaging horizontally the thermodynamic and water vapor equations as

$$Q_1 = \overline{\pi}\left(\frac{\partial\overline{\theta}}{\partial t} + \overline{\mathbf{V}}\cdot\nabla\overline{\theta} + \overline{w}\frac{\partial\overline{\theta}}{\partial z}\right) + \overline{Q}_R, \qquad (1)$$

$$Q_2 = -\frac{L_v}{C_P}\left(\frac{\partial\overline{q}_V}{\partial t} + \overline{\mathbf{V}}\cdot\nabla\overline{q}_V + \overline{w}\frac{\partial\overline{q}_V}{\partial z}\right). \qquad (2)$$

Here Q_1 and Q_2 can be calculated either from observations or from grid values in a large- or regional-scale prediction model; Q_1 and Q_2 can directly relate to the contributions of cloud effects, which can be explicitly estimated by CRMs (Soong and Tao 1980; Tao and Soong 1986; Tao and Simpson 1989; Krueger 1988; Tao et al. 1993; and many others):

$$Q_1 = \overline{\pi}\left(-\frac{1}{\overline{\rho}}\frac{\partial\overline{\rho}w'\theta'}{\partial z} - \mathbf{V}'\cdot\nabla\theta' + D_\theta\right) + \frac{L_v}{C_P}(c - e) + \frac{L_f}{C_P}(f - m) + \frac{L_s}{C_P}(d - s) + Q_R, \qquad (3)$$

$$Q_2 = \frac{L_v}{C_P}\left(\frac{1}{\overline{\rho}}\frac{\partial\overline{\rho}w'q'_V}{\partial z} + \mathbf{V}'\cdot\nabla q'_V + D_{q_V}\right) + \frac{L_v}{C_P}(c - e) + \frac{L_s}{C_P}(d - s). \qquad (4)$$

The overbars denote horizontal averages, and the primes indicate deviations from the horizontal averages. The variable $\overline{\rho}$ is the density, and $\overline{\pi} = (p/P_{oo})^{R/C_p}$ is the nondimensional pressure, where P is the dimensional pressure and p_{oo} the reference pressure taken to be 1000 mb; C_p is the specific heat of dry air at constant pressure, and R is the gas constant for dry air. The variables L_v, L_f, and L_s are the latent heats of condensation, fusion, and sublimation, respectively. The variables c, e, f, m,

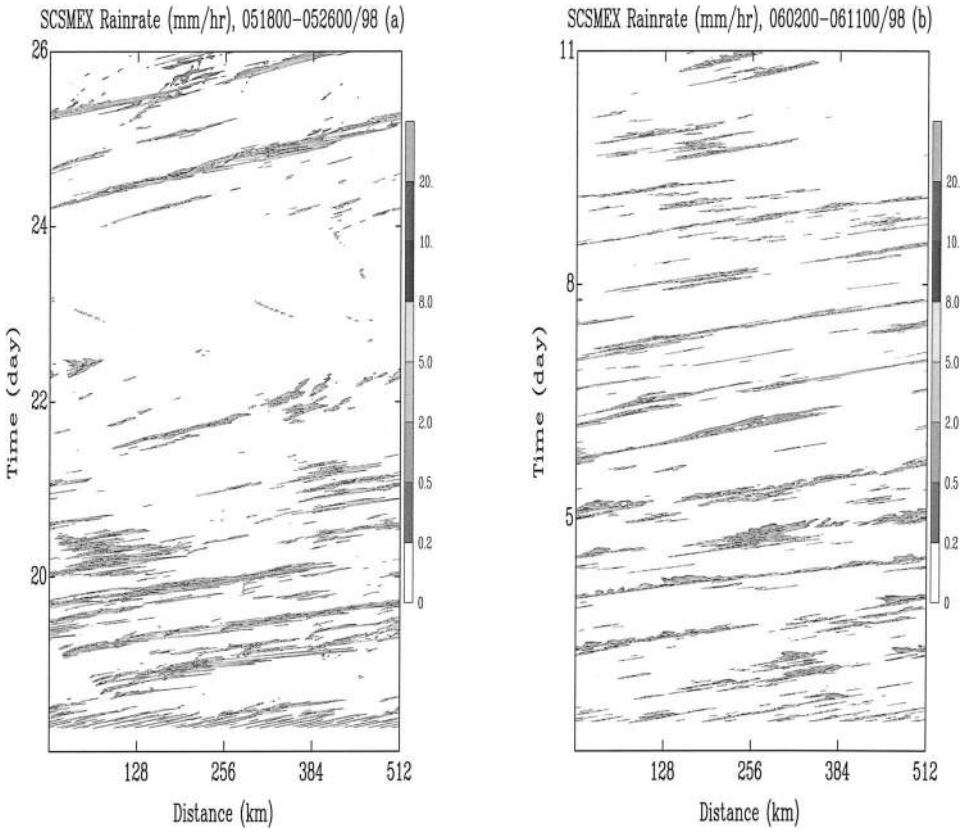

FIG. 5. Time sequence of the GCE model-estimated domain mean surface rainfall rate (mm h^{-1}) for (a) the 18–26 May 1998 period and (b) the 2–11 Jun 1998 period.

d, and *s* stand for the rates of condensation, evaporation of cloud droplets and raindrops, freezing of raindrops, melting of snow and graupel, deposition of ice particles, and sublimation of ice particles, respectively. The term Q_R is the cooling/heating rate associated with radiative processes. Also, the first terms on the right-hand side of (3) and (4) are the vertical eddy heat and moisture flux convergence, respectively.

Time series of the apparent heat source Q_1 diagnostically determined by soundings and explicitly calculated in the GCE model for the period 18–26 May 1998 are illustrated in Figs. 9a and 9b. The pattern of temporal variability corresponds well between the heating and the surface rainfall both for the estimated soundings and the GCE model. The model results, however, show more variability as expected. This is caused by the fact that diagnostically determined Q_1 was calculated using 6-hourly soundings. The GCE model estimates are based on 2-min statistics of cloud processes (i.e., condensation, evaporation, deposition and sublimation, melting and freezing rates). The GCE model did not capture the deep convection that occurred after May 24. This is because strong heating and drying are imposed at lower and middle levels (see Fig. 1) from the large-scale advective forcing during the period 23–24 May inhibiting the subsequent development of deep convection.[3] The model results showed that the convective profiles have heating throughout the troposphere with a simple maximum around 500–550 mb. In the stratiform region, heating is maximized in the upper troposphere (around 400 mb) while cooling prevails below the melting level.

There is also good agreement in terms of temporal variation related to major convective events found between the GCE simulation and the diagnostic sounding budget for the June period (Fig. 10). Model results indicate that there is no cooling below the freezing level for the convective event on 6–7 June. This is due to the strong moistening imposed by the large-scale advective forcing on 6 June (Fig. 1c), which suppresses the cooling from evaporation processes. Model results also indicate that there is stronger heating aloft (from deposition) and stronger cooling (from evaporation of rain) below in the stratiform region for both the May and June cases (see Figs. 9d and 10d). Generally, stronger deposition can generate more ice particles and more melting from ice

[3] An additional sensitivity test starting (initializing) the model on 24 May shows that deep convection could occur. Additional analysis also shows that larger temperature and water vapor errors occur during nonconvective and weaker convective events compared to stronger events.

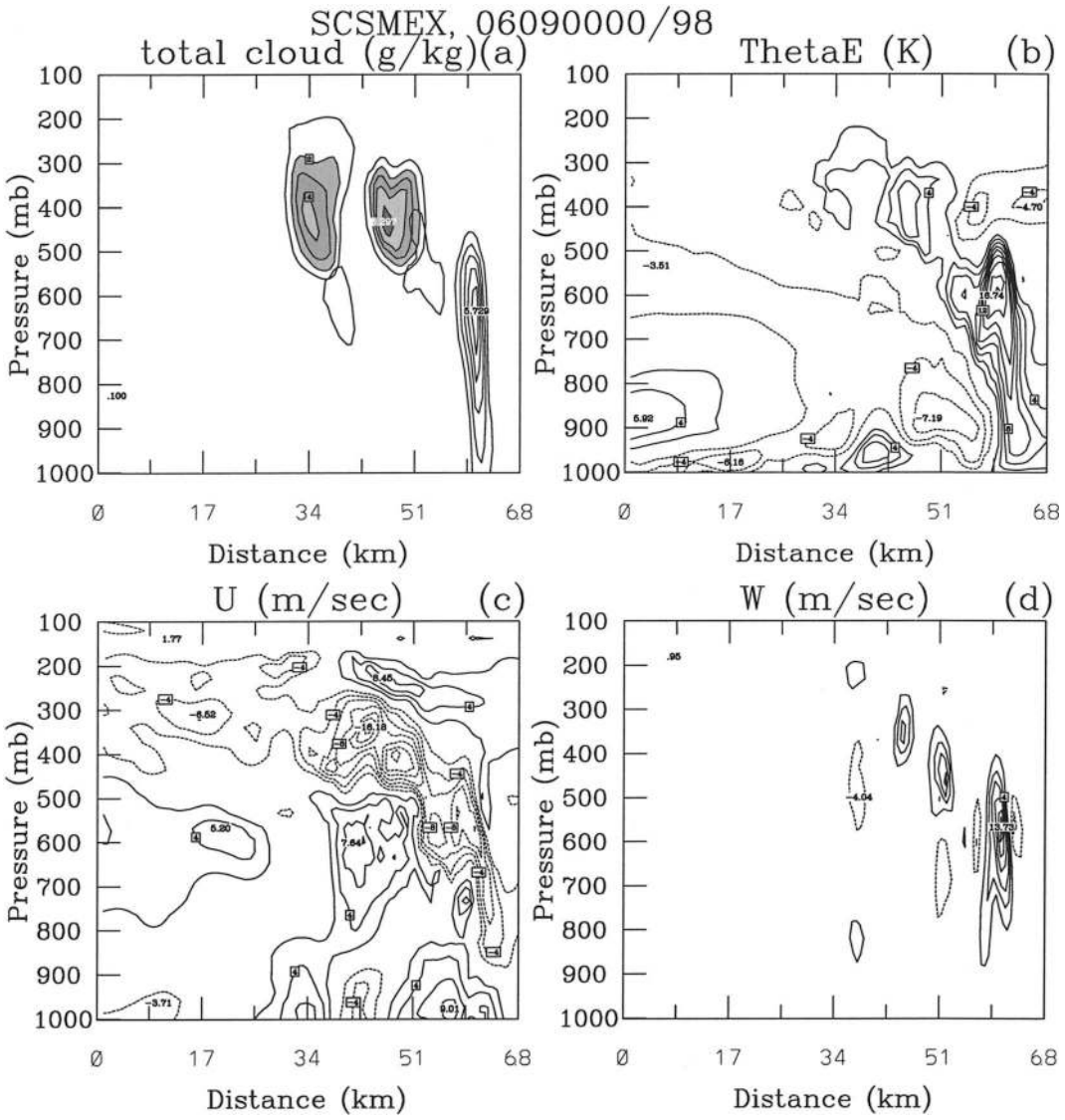

FIG. 6. Vertical cross sections of (a) the ice and liquid water content, (b) the equivalent potential temperature deviation, (c) the horizontal wind speed deviated from its horizontal mean, and (d) the *w* velocity after 7 days of simulation for the Jun SCSMEX case. The contour interval is 1 g kg^{-1}, 2 K, 2 m s^{-1}, and 2 m s^{-1} for (a), (b), (c), and (d), respectively. (e), (f), (g), (h) Same as (a), (b), (c), and (d), respectively, except for the May SCSMEX case after 3 days of simulation.

to rain. More evaporative cooling can occur with more rain.

As with the Q_1 budget, the model simulations capture the temporal variation of the observed Q_2 in both cases (Figs. 11 and 12). Again, the GCE model failed to produce the strong drying that occurred on 23–24 May as the Q_1 budget. Drying in the convective region is mainly due to the condensation/deposition processes (deplete moisture). The drying aloft and moistening (caused by evaporation) below occur in the stratiform region. Note that a drying was simulated in the planetary boundary layer in the stratiform region (Figs. 11d and 12d). In the planetary boundary layer, large-scale advective forcing in water vapor (Fig. 1) and latent heat fluxes from the ocean provide moisture. This could suppress the moistening effects due to rain evaporation. The model results do indicate that there is very little moistening through evaporation. The model results also indicate that the eddy flux convergence term (not microphysics) is responsible for this drying.

Time-averaged heating and moisture budgets for the two SCSMEX cases are shown in Fig. 13. The budgets diagnostically determined from soundings are also shown for comparison. For the May case, model-simulated Q_1 has a higher maximum heating level than observations. The June case has a better agreement with observations than the May case. Also note that the GCE-simulated latent heating profile is in good agreement

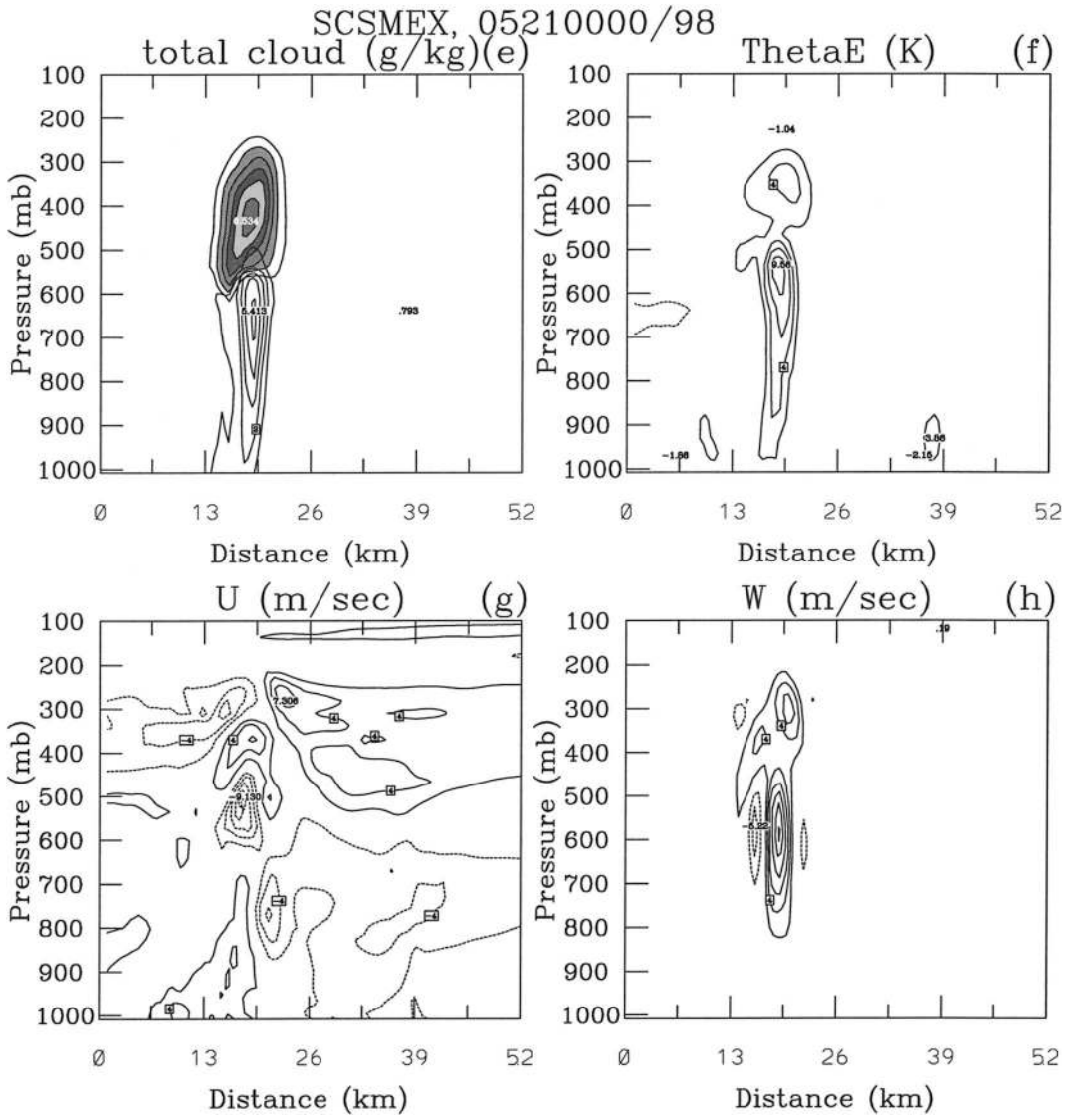

FIG. 6. (*Continued*)

with the sounding estimated for June case but not for May case even though the rainfall amounts differ from observations in both cases. Overall, model simulation has a better agreement with observations in the Q_2 than the Q_1 budget. The typical convective and stratiform heating/drying structures (or shapes) discussed in Houze (1982, 1997), Johnson (1984), and Chong and Hauser (1990) are well captured in the model except a large drying in the stratiform region at lower levels. The eddy flux convergence term is responsible for this drying (Figs. 11 and 12).

Figures 14a and 14b show the net condensation, the net radiation, and vertical eddy heat flux convergence in the Q_1 budget for both the May and June cases. The vertical eddy flux convergence term includes both cloud-scale and subgrid-scale (turbulence) effects. The net condensation and the large-scale forcing are the largest terms and are opposites. The net radiation is a cooling that is about 20%–30% of the condensational heating. The eddy heat flux convergence basically acts to redistribute heat vertically and it cannot be neglected in the Q_1 budget in the middle levels (5-km level). This feature is related to the localized cooling by the melting processes. The eddy heat flux transports heat into the melting layer to compensate for the loss of heating from the melting process. This eddy transport term can also transport heat above the melting caused by the localized freezing processes (i.e., Fig. 14b). More melting and freezing in the June case produces a larger eddy heat flux convergence. Previous model results indicated that the eddy heat flux convergence term in temperature is very small except below cloud base

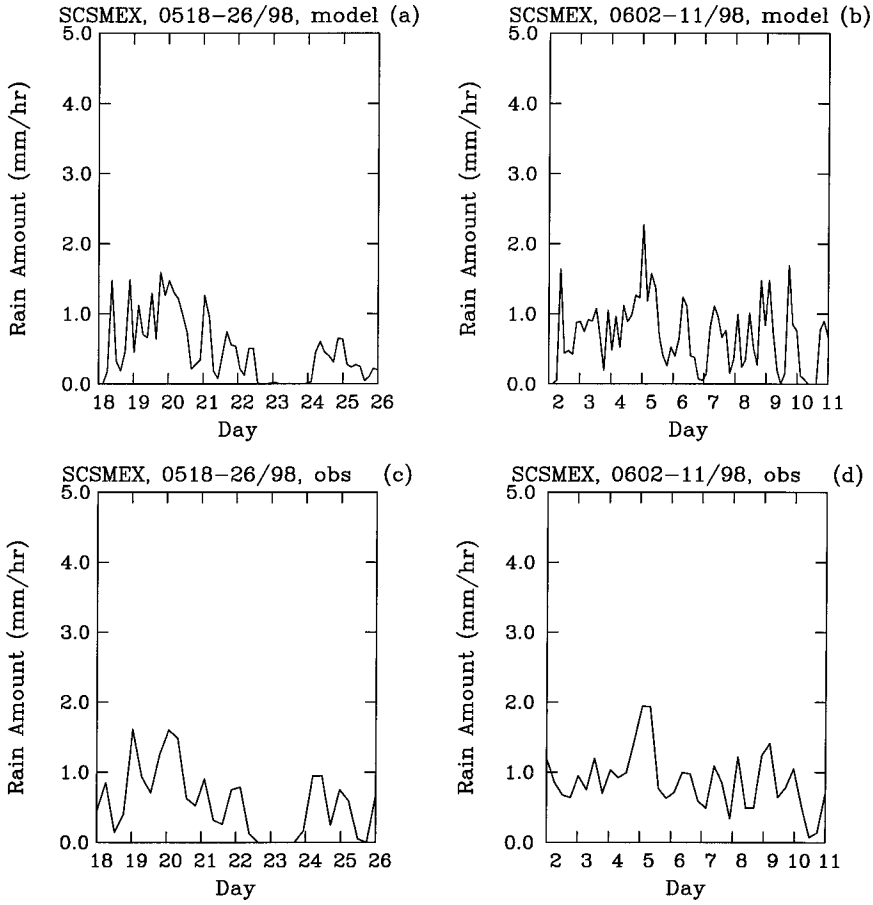

FIG. 7. Time sequence of the GCE model–estimated domain-mean surface rainfall rate (mm h^{-1}) for (a) 18–26 May and (b) 2–11 Jun 1998. (c), (d) Rainfall estimated using Q_2 budget.

compared to other terms (Soong and Tao 1980; Tao and Soong 1986; Krueger 1988). The lack of ice processes in these previous modeling studies is the reason for this difference.

For the Q_2 budget, the GCE model results indicated that the net condensation and the imposed large-scale advective water vapor are in opposition. The vertical eddy convergence/divergence of moisture by clouds is quite important for the Q_2 budget. It simply transports moisture from the lower to upper troposphere. The vertical eddy convergence term is the same magnitude as the large-scale advective forcing above the 8-km level. Also, it produces much drying in the lower troposphere that counteracts the large-scale moistening effect. The eddy moisture flux convergence also has a local maximum at middle levels (i.e., Fig. 14d). This feature is in response to a maximum in condensation (loss of moisture; see Fig. 15). The larger contribution of the vertical eddy convergence/divergence term in the Q_2 (water vapor) than the Q_1 (temperature) budgets is the major reason for Q_1 and Q_2 decoupling (the level of maximum values in the Q_1 and Q_2 profiles is not at the same level).

Figure 15 shows the simulated individual domain- and time-averaged accumulated microphysical processes (condensation, evaporation, deposition, sublimation, melting, and freezing) associated with May and June cases. Both condensation and evaporation are the largest terms in both cases. The evaporation and sublimation, respectively, are about one-third of the condensation and deposition. Both melting and freezing are small compared to condensation, evaporation, deposition, and sublimation. However, the melting is the process responsible for the local minimum of net condensation heating (Figs. 14a and 14b), even though the condensation shows a maximum at the 5-km level.

There are several differences between the May and June cases. The first one is that convection is more vigorous and has a higher temporal variation in June than May. The convective heating is stronger and occurs at a higher altitude in convective systems in June. The cooling in the stratiform region is also much stronger in June than in May. This is because the convective systems have more mesoscale organization in June (Fig. 6). All terms in the Q_1 and Q_2 budgets are larger in the June case than May case.

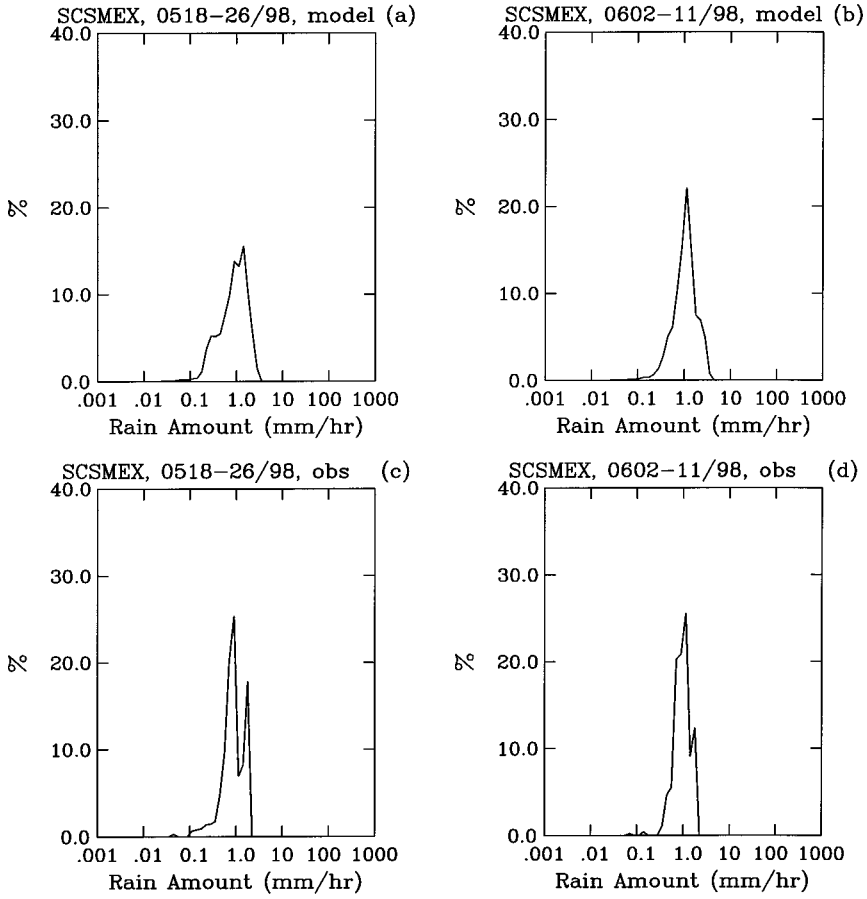

FIG. 8. Probability distribution of simulated rainfall for the (a) May and (b) Jun SCSMEX cases. (c), (d) Same as (a) and (b), except for estimated rainfall by sounding.

c. Atmospheric energy budgets

Horizontal and vertical integration of the equations for temperature, water vapor (q_v), and moist static energy $h(h = C_pT + L_vq_v + gz)$ over the entire model domain yields

$$C_p\left\langle\frac{\partial\overline{T}}{\partial t}\right\rangle = \langle L_v(\overline{c} - \overline{e}) + L_f(\overline{f} - \overline{m}) + L_s(\overline{d} - \overline{s})\rangle - C_p\left\langle\frac{\partial\overline{\theta}}{\partial t}\right\rangle_{\text{L.S.}} + \overline{Q}_R + C_p\overline{H}_s, \quad (5)$$

$$L_v\left\langle\frac{\partial\overline{q}_v}{\partial t}\right\rangle = -L_v\langle(\overline{c} - \overline{e}) + (\overline{d} - \overline{s})\rangle - L_v\left\langle\frac{\partial\overline{q}_v}{\partial t}\right\rangle_{\text{L.S.}} + L_v\overline{E}_o, \quad (6)$$

$$\left\langle\frac{\partial\overline{h}}{\partial t}\right\rangle = \langle L_F(\overline{f} - \overline{m}) + (L_s - L_v)(\overline{d} - \overline{s})\rangle - \left(C_p\left\langle\frac{\partial\overline{\theta}}{\partial t}\right\rangle_{\text{L.S.}} + L_v\left\langle\frac{\partial\overline{q}_v}{\partial t}\right\rangle_{\text{L.S.}}\right) + \overline{Q}_R + C_p\overline{H}_s + L_v\overline{E}_o, \quad (7)$$

where $-\langle\partial\overline{\theta}/\partial t\rangle_{\text{L.S.}}$ and $-\langle\partial\overline{q}_v/\partial t\rangle_{\text{L.S.}}$ are the large-scale advective cooling and moistening, and E_o and H_s are the latent and sensible heat fluxes from the ocean surface. The similarities and differences in terms of large-scale forcing, surface fluxes, and radiation upon precipitation (net condensation) between two cases can be identified. In addition, the physical processes responsible for the precipitation processes in each case can be quantified.

Table 3 lists the temperature budget for the May and June cases. In both runs, the largest two terms in the temperature budget are net condensation (heating) and imposed large-scale forcing (cooling). These two terms are opposite in sign, however. This is also true for the water vapor budget (Table 4). Soong and Tao (1980) performed experiments with different magnitudes of large-scale forcing and found that the larger the large-scale forcing (cooling/moistening), the larger the net condensation (heating/drying). They hypothesized that the effect of cloud microphysics is simply a response to the ''imposed large-scale forcing in temperature and water vapor.'' The sensible heat flux is two to three orders of magnitude smaller than the net condensation and large-scale forcing. The latent heat flux is about 17% and 5%,

TABLE 2. Domain-averaged surface rainfall amounts (mm day^{-1}) and stratiform percentage for both the May and Jun cases. Rainfall amounts and stratiform estimated by TRMM PR, TMI, and sounding network are also shown.

	GCE rainfall/stratiform (%)	Sounding rainfall	PR rainfall/stratiform (%)	TMI rainfall/stratiform (%)	GPCP rainfall
18–26 May 1998	11.14/49	13.00	10.56/33	24.22/26	14.22
2–11 Jun 1998	16.46/38	20.71	17.93/44	31.95/31	16.38

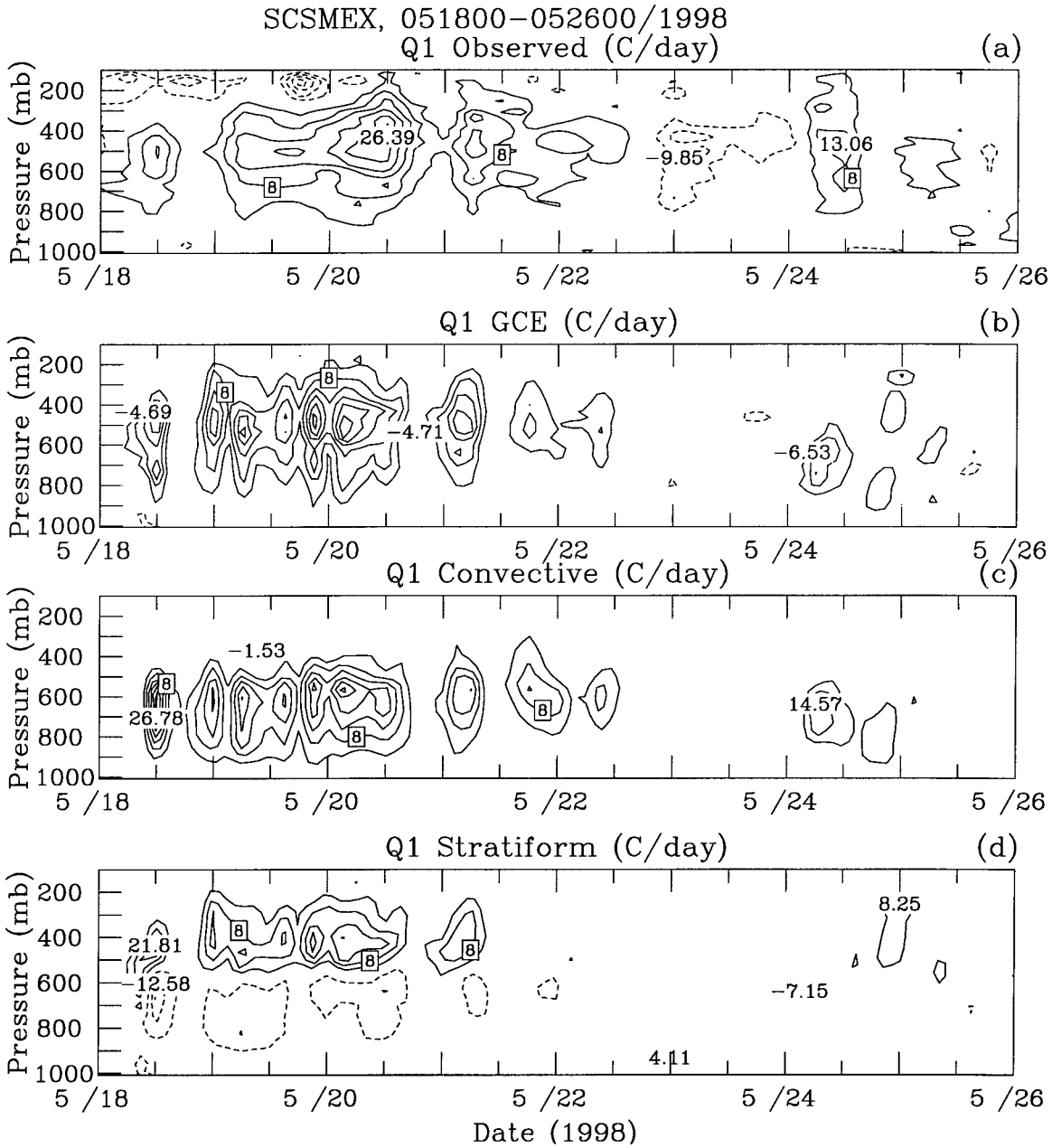

FIG. 9. Evolution of the domain-average apparent heat source (Q_1) for SCSMEX for the 8-day period 18–26 May 1998. (a) Derived diagnostically from soundings (Johnson and Ciesielski 2002). (b) Simulated from the GCE model. The GCE model simulated Q1 over (c) the convective region and (d) the stratiform region. The contour interval is 4°C day^{-1} for (a), (b), (c), and (d).

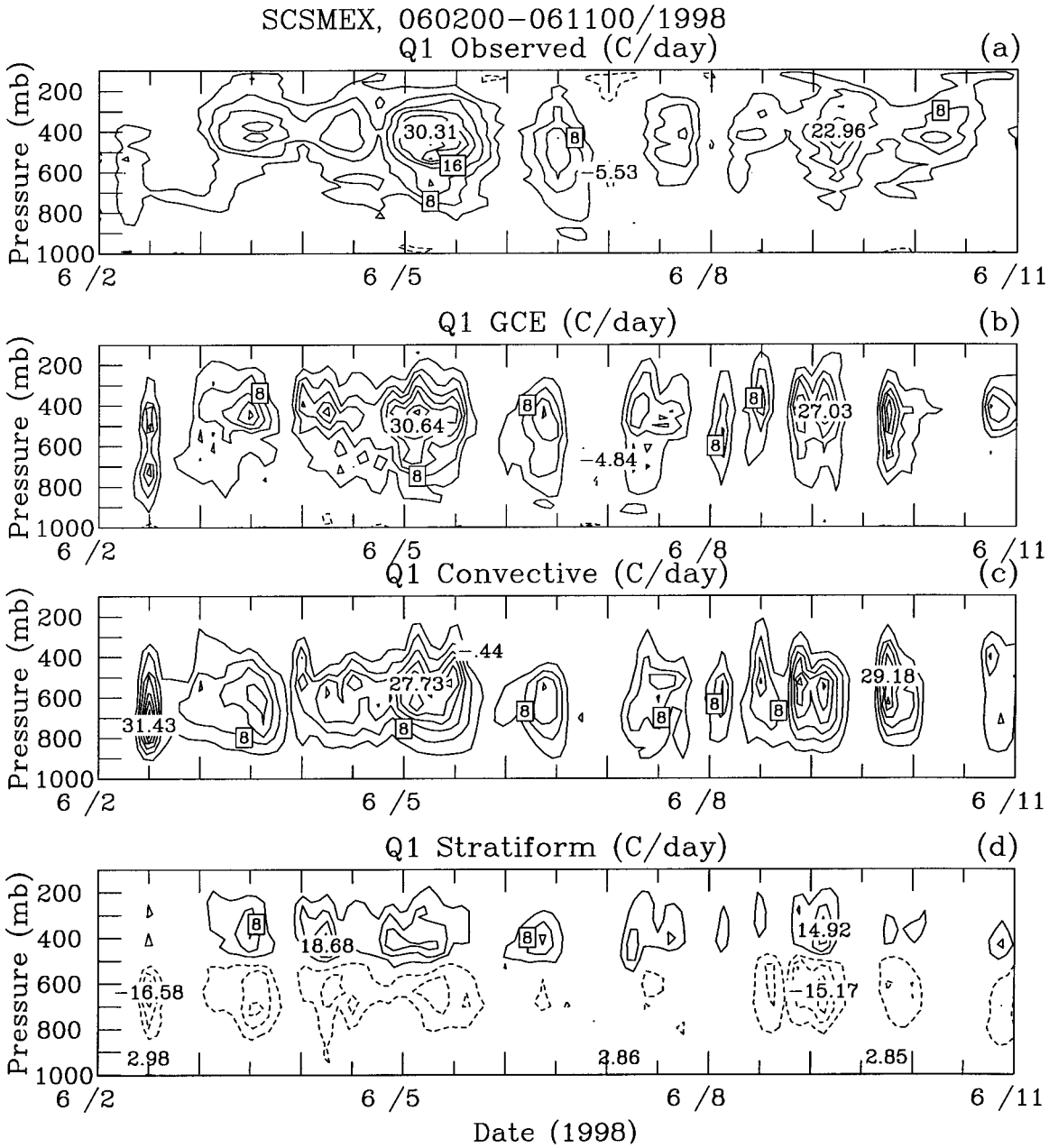

FIG. 10. Same as Fig. 9, except for the 2–11 Jun 1998 period.

respectively, of large-scale forcing in the May and June cases. Net radiation results in cooling and is about 34% and 25%, respectively, of the net condensation for the May and June cases. This result clearly suggests that radiation plays an important role in the energy budget and precipitation processes for both cases.

There are several differences between the May and June cases. The first one is that the contribution by radiation and latent heat fluxes to precipitation is larger in the May case (Tables 3 and 4). The mean SST is quite similar between May and June (27.99° versus 28.2°C). However, the large-scale advective forcing in water vapor is very large in the lower troposphere and generates a moist boundary layer in June (Fig. 2b). This reduces the contribution from latent heat fluxes from the ocean in the June case. The smaller large-scale temperature forcing in the May case is the reason for the larger contribution from radiation. Another difference is that net condensation is smaller than the large-scale water vapor forcing in the June case but not in the May case.

Temperature and water vapor are closely related. Evaporative cooling/condensational heating is a source/sink for the water vapor field. On the other hand, latent

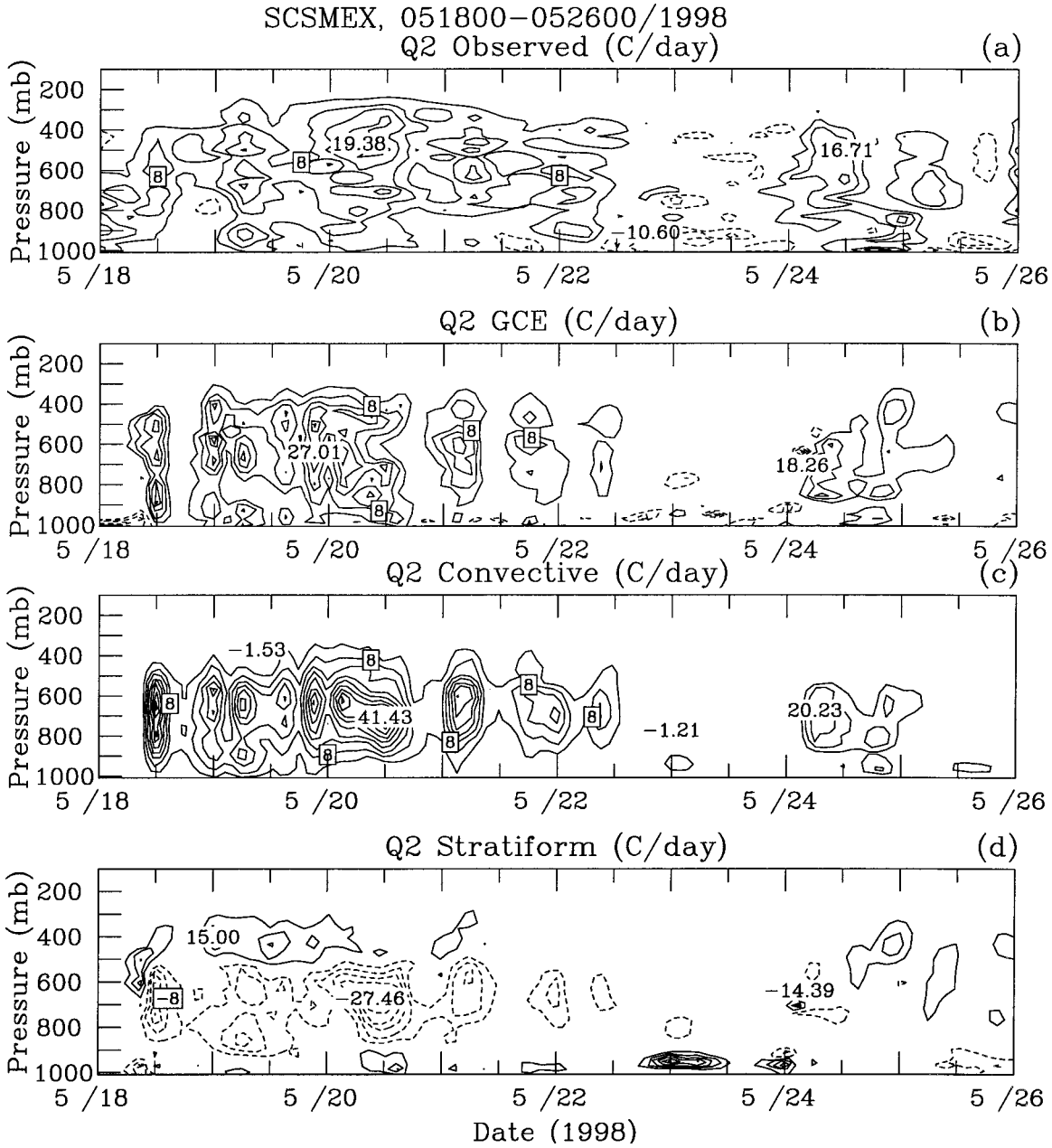

FIG. 11. Same as Fig. 9, except for the Q_2 budget.

heat flux from the ocean surface can provide water vapor for condensation heating. The moist static energy budget (Table 5) provides some additional information on the physical processes for both SCSMEX cases. The microphysical processes in the moist static energy budget are melting (cooling), freezing (heating), and the product between the latent heat of fusion and the net deposition (deposition minus sublimation)[4] [Eq. (7)]. These microphysical processes and the sensible heat fluxes are the smallest terms in the moist static energy budget. The local change term is negative for the May case but positive in the June case. The large-scale advective forcing is larger (smaller) than the radiational cooling for the June (May) case. This effect contributes to a positive (negative) local change term in the June (May) case. For May, the negative local change in moist static energy is mainly from temperature (through radiation), not moisture. For June, the positive bias is from the large-scale water vapor forcing. The relationships between latent heat fluxes and the local change term are the opposite between the May and June cases. In a sep-

[4] This term is usually positive, that is, to release heating in the model simulation (Fig. 15). This term is zero in the ice-free case.

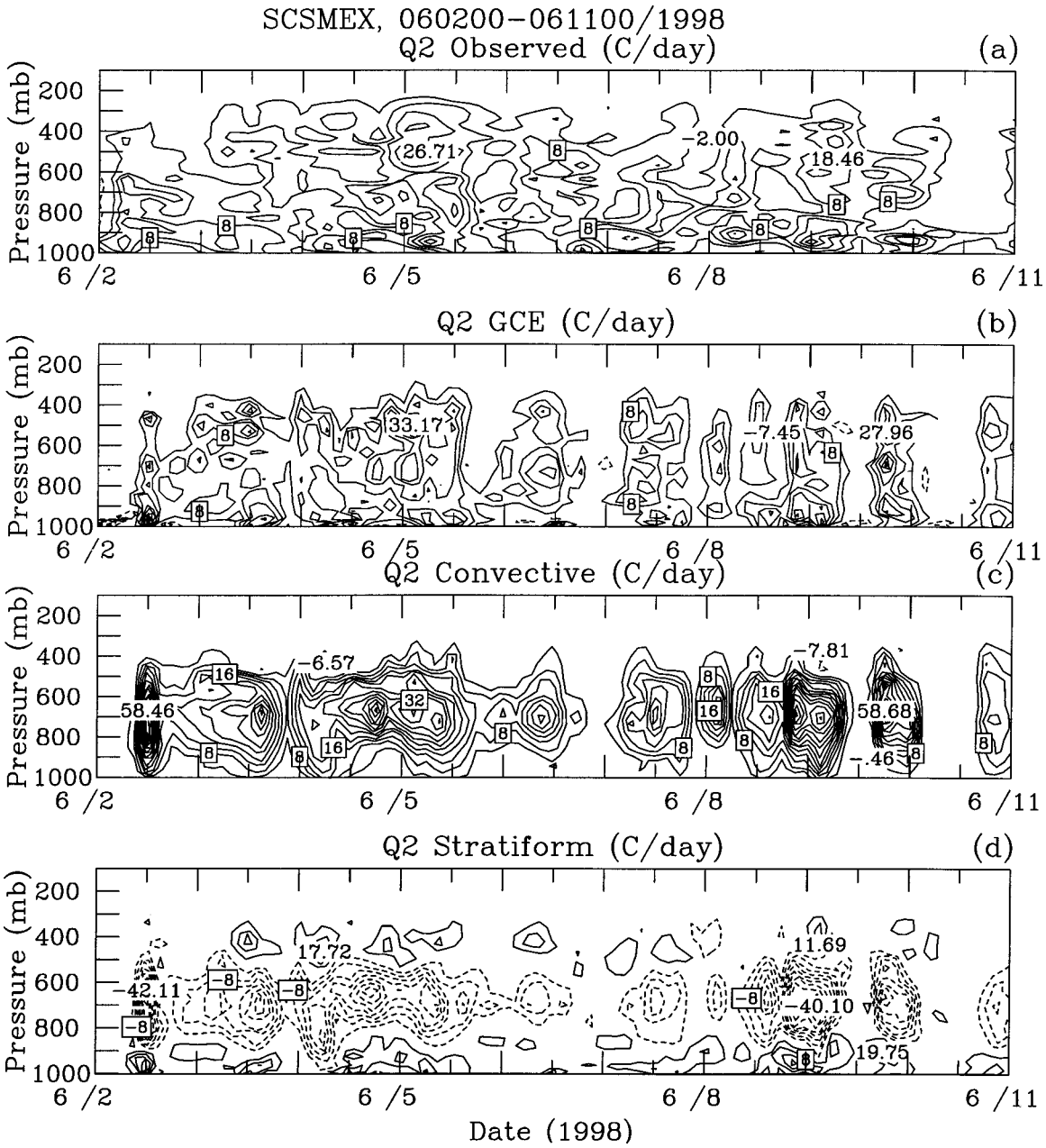

FIG. 12. Same as Fig. 10, except for the Q_2 budget.

arate paper (Tao et al. 2003, manuscript submitted to *J. Atmos. Sci.*), the energy budget and its relationship to the precipitation efficiency of convective systems during TOGA COARE, GATE, the Atmospheric Radiation Measurement (ARM) program, and SCSMEX will be examined and compared.

5. Sensitivity tests

a. Cloud–radiation interaction

A sensitivity test is performed to examine the impact of cloud–radiation interaction on precipitation processes. In the test, the horizontal domain-averaged cloud fields are used to calculate cloud optical properties. Then, the radiative heating/cooling is applied horizontally uniform as with the imposed large-scale advective forcing. In this way, any inhomogeneities associated with cloud–radiation interaction are eliminated, and the test can be interpreted as a large-scale cloud–radiation interaction case.

The model results indicate that cloud organization, as well as stratiform rain percentage (Tables 2 and 6), does not change much in the sensitivity test compared to the control run for both the May and June cases. The large-

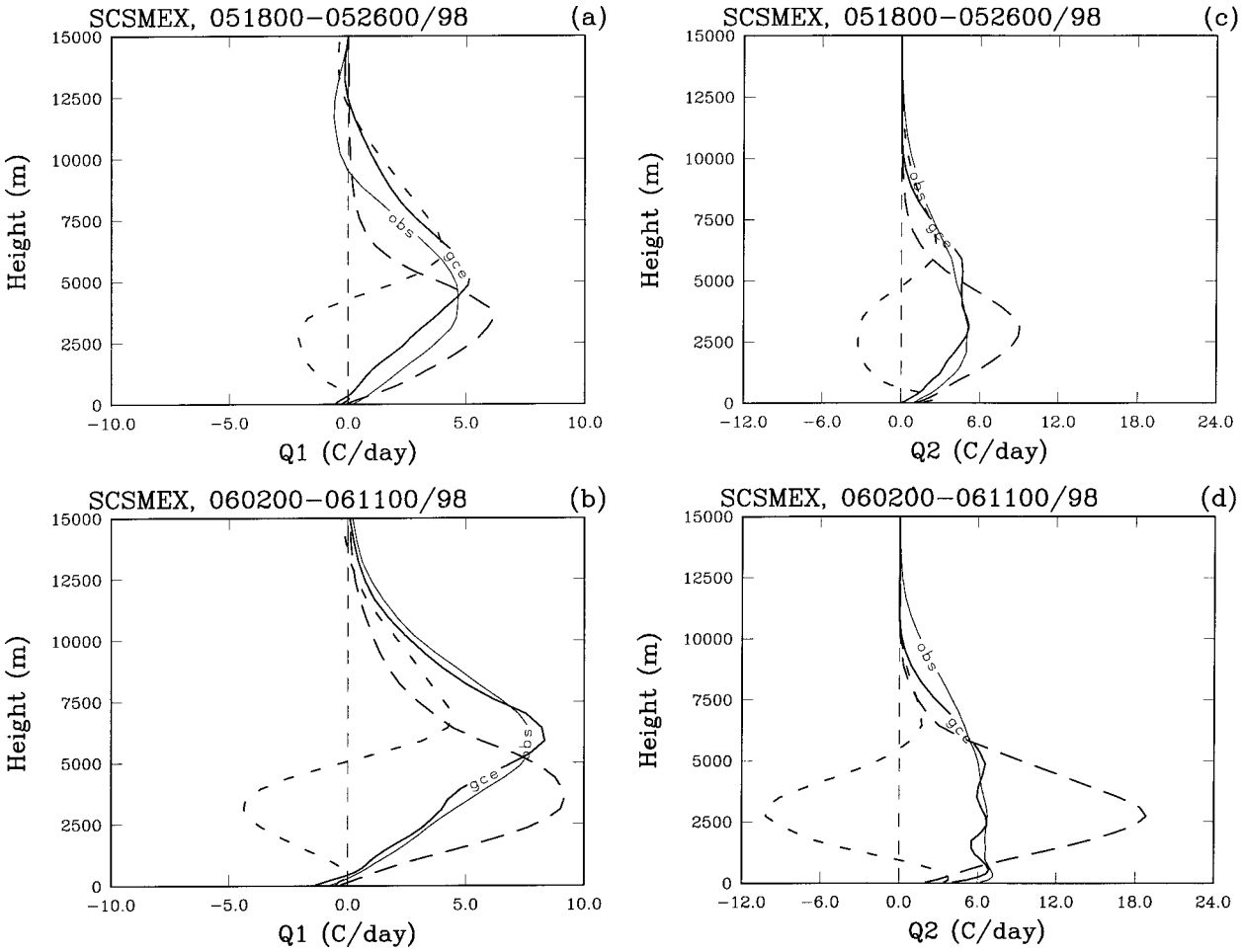

FIG. 13. Eight-day average profiles of (a) Q_1 (°C day^{-1}) and (c) Q_2 (°C day^{-1}) for the period 18–26 May 1998. GCE model simulated Q_1 for the convective and stratiform regions are shown as dashed and dotted lines, respectively. Diagnostically derived profiles are also shown. (b), (d) Same as (a) and (c) except for the 9-day period 2–11 Jun 1998.

scale mean *u* wind is the same between the sensitivity test and the control run. This explains why the different treatment for cloud–radiation interaction does not significantly impact convective organization. However, surface rainfall is reduced by 7.5% and 8.8%, respectively, compared to the control runs for the May and June cases (Tables 2 and 6). The temperature and water vapor budgets for the sensitivity runs reveal that the net radiative cooling is reduced by 8.8% and 11% with respect to net condensation, compared to the control runs for May and June, respectively.

Figure 16 shows the time- and domain-averaged shortwave heating and longwave cooling profiles for both the control runs and the sensitivity tests. Both longwave cooling and shortwave heating are reduced in the lower and upper troposphere in the sensitivity runs compared to the control runs for both the May and June cases. Net radiative cooling in the lower troposphere is slightly reduced by about 0.2°C day^{-1} in the sensitivity runs. The average large-scale advective cooling in the lower troposphere is about 2°–3°C day^{-1} (Fig. 2). A 10% reduction in net condensation and rainfall in the sensitivity tests is consistent with the reduction in net radiative cooling. Latent heat fluxes are also reduced in the sensitivity runs but by less than 2% with respect to net condensation. Therefore, the reduction in net radiative cooling is the main physical process responsible for the reduction in rainfall. This is in good agreement with Tao et al. (1996) and Sui et al. (1998).

Xu and Randall (1995), Fu et al. (1995), and Petch and Gray (2001) suggested that the destabilization mechanism could be important for prolonging the life span of high anvil clouds (around 10 km). Xu and Randall (1995) showed that this direct cloud destabilization does not have any impact on surface precipitation. Petch and Gray (2001) showed that cloud–radiation interaction could increase precipitation (~5%) compared to equivalent runs without radiation parameterization. Their results also showed that cloud mass fluxes and cloud amounts tend to increase when the radiation is applied as a domain average (they gave no information as to whether or not surface precipitation or surface

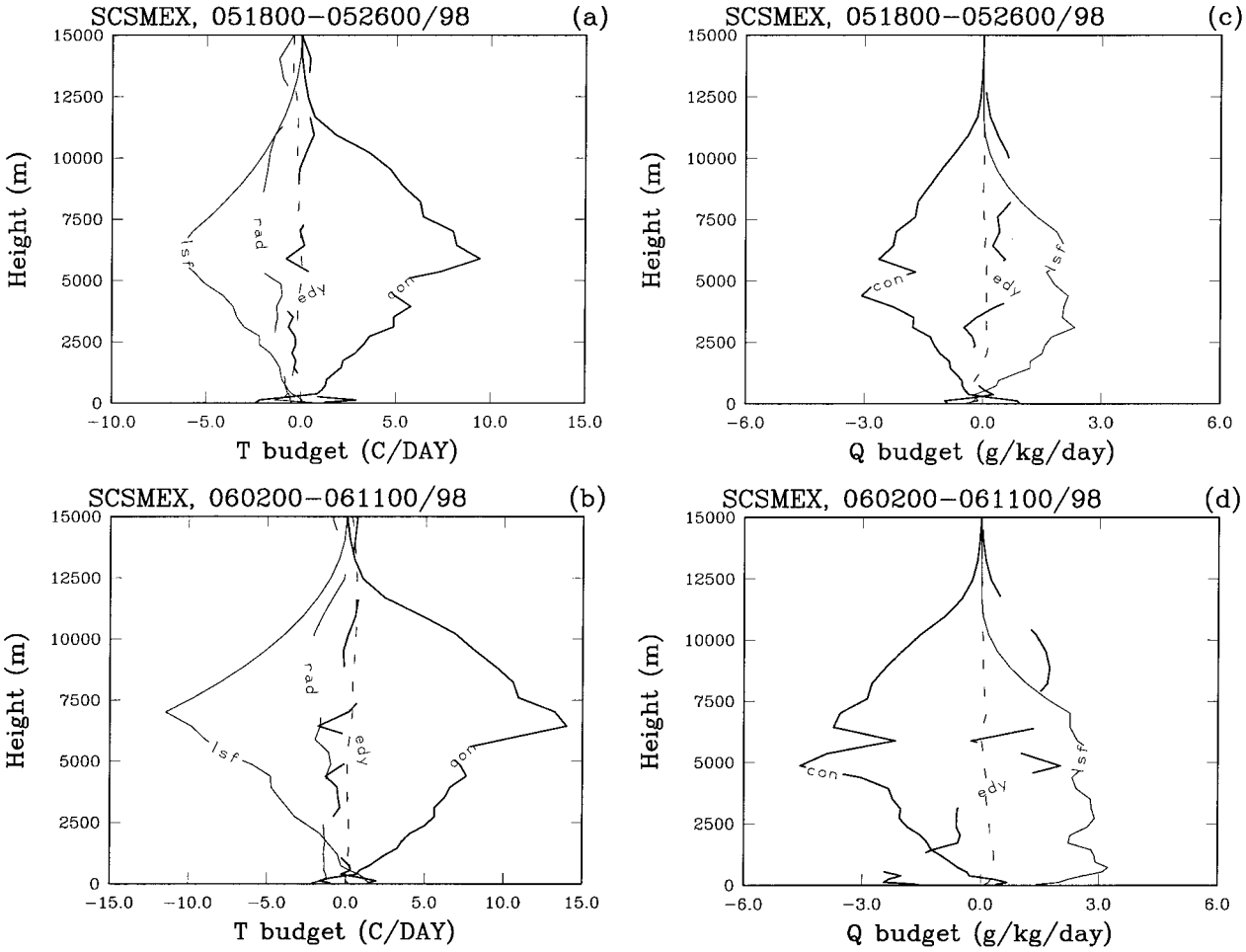

FIG. 14. (a) Heating and (c) moisture budgets for the May SCSMEX case averaged over the 8-day simulation time. Contributions from net condensation (condensation + deposition-evaporation-sublimation, in thick solid line marked con) and the total vertical eddy-flux convergence [includes both cloud-scale and subgrid-scale (turbulence) effects, in thick dashed line marked edy] are shown. The imposed large-scale advective forcing (thin solid line marked lsf) and net radiation (thin dashed line marked rad) are also shown. (b), (d) Same as (a) and (c), except for the Jun case.

fluxes are enhanced). They suggest that in periods when new convection is developing, radiative cooling is stronger in the interactive runs than in the ''domain-mean'' runs. The instability of the atmosphere is therefore greater and can lead to stronger convection. However, the small difference (a few tenths of a degree; see Fig. 16) in the radiative heating/cooling rates cannot increase the instability of the atmosphere.

Modeling studies (Fu et al. 1995; Miller and Frank 1993) have also indicated that more surface precipitation can be generated in runs with constant clear-air radiative cooling than without. In addition, previous modeling results (Chin 1994; Chin et al. 1995; Miller and Frank 1993; Tao et al. 1996) indicated that solar radiative processes can reduce precipitation processes. However, the amount of increase or decrease in surface precipitation varies quite significantly among these different modeling studies, but only in regard to the tropical convective systems and not the midlatitude systems. One possible explanation is that large-scale forcing (lifting) was needed in some of these different tropical convective system studies. The imposed lifting varied from 2 to 14 cm s^{-1} in magnitude and was applied continuously or discontinuously in time among the different studies (see Table 8 in Tao 2003). Please see Tao (2003) for reviews and discussions on using cloud-resolving models to examine the impact of radiative processes on precipitation in convective systems.

b. Microphysical processes

1) WARM RAIN PROCESSES

The importance of ice microphysics to precipitation formation has long been known (please see a brief review in McCumber et al. 1991). The importance of ice microphysics to the formation of stratiform rain has been identified in previous cloud modeling studies (Fov-

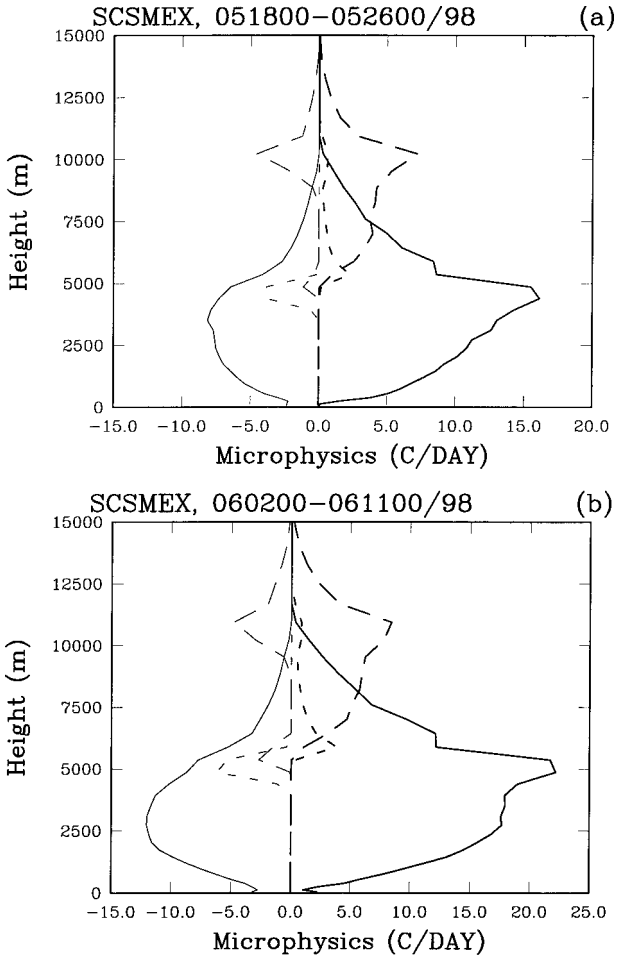

FIG. 15. (a) Vertical profiles of domain- and time-averaged accumulated condensation (thick solid line), evaporation (thin solid line), deposition (thick dashed line), sublimation (thin dashed line), melting (thin dotted line), and freezing (thick dotted line) for the May SCSMEX case. (b) Same as (a), except for the Jun case.

ell and Ogura 1988; Tao and Simpson 1989; and others). A no-ice phase version of the GCE model, with a Kessler-type two-category liquid water microphysics, is used to simulate the SCSMEX cases. One of the major differences between the ice runs and the ice-free runs is that heavier precipitation accounts for a larger portion of the total rain in the ice-free runs. Only 42% and 28% of the rain is characterized as stratiform for the May and June cases, respectively (Table 6). This is a reduction of 6%–10% compared to the control runs. Another major difference is that less (16.5%–18% reduction) total rain is produced in the ice-free runs (Tables 2 and 6). These results are consistent with previous modeling studies (i.e., Fovell and Ogura 1988; Tao and Simpson 1989; McCumber et al. 1991). Also, is found that the contribution of eddy heat flux convergence/divergence in the Q_1 budget is very small and can be neglected at middle levels in the ice-free runs. This is because the localized cooling/heating by the melting/freezing process is not allowed in the no-ice runs.

TABLE 4. Same as in Table 3, except for the water budgets. Net condensation is the sum of condensation, deposition, evaporation, and sublimation of cloud. Large-scale forcing is the imposed large-scale advection effect on water vapor, and dq_v/dt is the local time change of water vapor. Units are mm day^{-1}. To convert mm day^{-1} to W m^{-2}, multiply by a factor of 28.9.

	dq_v/dt	Net condensation	Large-scale forcing	Latent heat fluxes
18–26 May 1998	−0.15	−11.23	9.81	1.27
2–11 Jun 1998	1.12	−16.45	16.84	0.73

The temperature and water vapor budgets for the sensitivity runs reveal that net radiative cooling is reduced to 0.0 (identical solar heating and longwave cooling rates) and −16.4 W m^{-2} for May and June, respectively (not shown). The cloud water is assumed to be monodisperse and to advect with airflow, having no appreciable terminal velocity of its own. Consequently, thick anvil clouds are simulated in the ice-free runs (Fig. 17). For high, thick anvil clouds, the effects on solar heating and longwave cooling are both large and largely offset each other (solar reflection is large, and longwave emission is low). As discussed in previous sensitivity tests, the reduction in net radiative cooling can decrease the net condensation and rainfall production. Also latent heat fluxes are reduced and that is because a warmer and more humid boundary layer compared to the control runs is simulated. That is caused by less net condensation (condensation minus evaporation) in the boundary layer while large-scale advective forcing in water vapor still supplies abundant moisture.

2) ICE MODIFICATION

Recently, the conversion of cloud ice to snow in the Goddard three-class ice microphysics (3ICE) schemes was modified (see Tao et al. 2003). An important process in the budget for cloud ice is the conversion of cloud

TABLE 3. Temperature budgets for the 18–26 May and 2–11 Jun 1998 cases. Net condensation is the sum of condensation, deposition, evaporation, sublimation, freezing, and melting of cloud. Large-scale forcing is the imposed large-scale advective effect on temperature, and dT/dt is the local time change of temperature. Longwave cooling, shortwave heating, and their net radiative processes are shown in Q_R. Units are °C day^{-1}. To convert °C day^{-1} to W m^{-2}, multiply by a factor of 116.

	dT/dt	Net condensation	Large-scale forcing	Net Q_R = SW − LW	Sensible heat fluxes
18–26 May 1998	−0.12	2.83	−2.03	−0.95 = 0.70 − 1.65	0.03
2–11 Jun 1998	0.26	4.17	−2.88	−1.04 = 0.69 − 1.73	0.01

TABLE 5. Same as in Table 4, except for the moist static energy budget. Units are W m^{-2}.

	$D(C_pT + L_vQ_v)$	Net condensation	Large-scale forcing	Net Q_R	Sensible heat fluxes	Latent heat fluxes
18–26 May 1998	−18.0	2.84	48.8	−110.7	4.2	36.85
2–11 Jun 1998	62.4	3.55	156.6	−119.9	1.07	21.11

ice to snow as the ice crystals grow by vapor deposition in the presence of cloud water, usually referred to as the Bergeron process and designated as the production of snow from ice (PSFI) by Lin et al. (1983). As described in Tao et al. (2003), the formulation generally used in the parameterization is independent of relative humidity, which causes ice to be converted to snow even when the air is subsaturated with respect to ice. Two alternative formulations are proposed. In the first, the original formula is simply multiplied by an empirically derived relative humidity dependency factor so that PSFI diminishes as the relative humidity approaches the ice saturation value. The second alternative formulation is derived directly from the equation for depositional growth of cloud ice (Rutledge and Hobbs 1984) used in the model. This formulation causes PSFI to diminish as the relative humidity approaches the ice saturation value, but also ensures physical consistency with the parameterization of depositional growth of cloud ice used in the model. The two alternative formulations produce relatively similar results since simulated ice clouds over the tropical oceans often have vapor mixing ratios near the ice saturation value so that PSFI is very small. Another modification is the accretion of snow by graupel. This conversion process will be reduced under the presence of liquid water. This modification can reduce unrealistically abundant graupel in the stratiform region.

Figure 18 shows the simulated domain- and time-averaged cloud ice, snow, and graupel for the June case using the original (Figs. 18a,b,c) and the modified 3ICE scheme (Figs. 18d,e,f). The main differences are an increase in cloud-top height and an increase in the cloud ice mixing ratios, particularly at upper levels in the cloud, using the new formulation of PSFI. Another difference is a significant increase in snow and decrease in graupel in the new formulation of snow conversion to graupel. This increase in snow and decrease in graupel occurs in the stratiform region. Similar results are also found for the May case.

The model results indicate that cloud organization and stratiform rain percentage (Tables 2 and 6) are not affected very much due to the change in the microphysics. Again, this is because the same large-scale mean u wind is imposed for the sensitivity tests and control runs. The surface rainfall, however, is reduced 13% and 8.5%, respectively, compared to the control runs in the May and June cases (Tables 2 and 6). The temperature and water vapor budgets for the sensitivity runs indicate that longwave radiative cooling is reduced by 16% and 11% with respect to net condensation, compared to the control runs for May and June, respectively. Shortwave radiative heating is not altered by the different microphysical scheme, however. The higher cloud tops in the new PSFI formulation affect the longwave radiation much more than the shortwave radiation. Latent heat fluxes are only slightly reduced (less than 0.5%) with respect to net condensation in the sensitivity runs. The reduction in longwave radiative cooling is the main physical process responsible for the reduction in rainfall.

Petch and Gray (2001) indicated that surface precipitation, cloud mass fluxes, and total hydrometeors are very similar for three different microphysical schemes when no radiation is included, but with interactive radiation there are differences (mainly the cloud ice content is increased significantly). The total surface precipitation and cloud mass fluxes are still quite similar for the three different microphysical schemes, even with interactive radiation. Their results are different from the current study. A more detailed model comparison on cloud–radiation interaction as recommended by the GCSS is needed. The GCSS model intercomparison will focus on cloud–radiation interaction and air–sea interaction by performing offline calculations (see http://rsd.gsfc.nasa.gov/users/djohnson/gcsswg4).

c. Wind shear

The final sensitivity test addresses the impact of the mean wind shear profile on precipitation processes. In the sensitivity test, the horizontal wind components u and v set their respective surface values and held constant with height. Components u and v are allowed to change with time as observed using the same nudging

TABLE 6. Same as in Table 2, except for the sensitivity tests.

	Uniform radiation		Warm rain		Modified 3ICE scheme		Uniform u wind	
	Rainfall (mm day^{-1})	Stratiform (%)	Rainfall (mm day^{-1})	Stratiform (%)	Rainfall (mm day^{-1})	Stratiform (%)	Rainfall (mm day^{-1})	Stratiform (%)
18–26 May 1998	10.30	47	9.10	42	9.64	49	11.25	43
2–11 Jun 1998	15.01	35	13.74	28	15.22	36	16.42	33

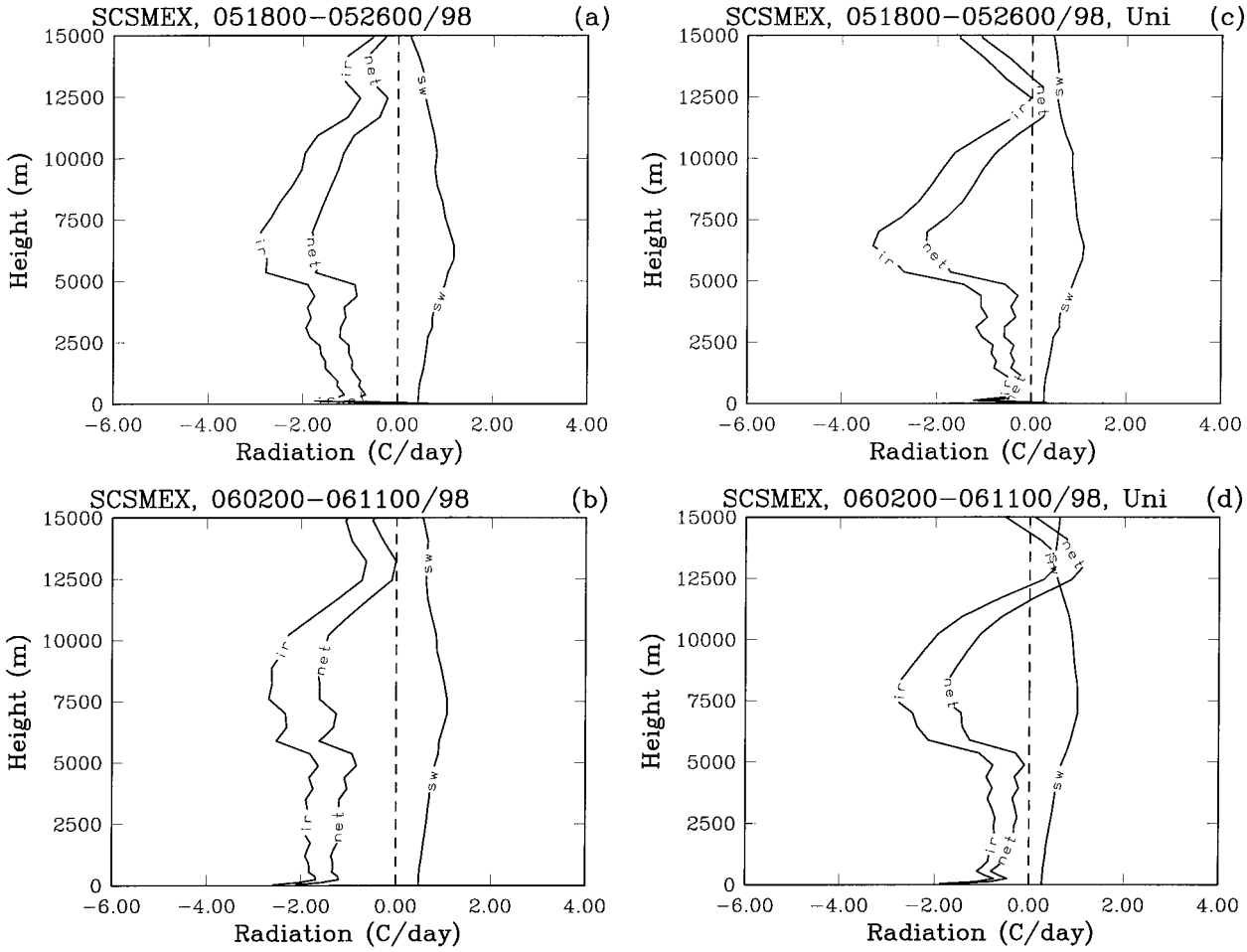

FIG. 16. Vertical profiles of time- and domain-averaged radiation (total, longwave cooling, and shortwave heating) for the (a) May and (b) Jun SCSMEX cases. (c), (d) Same as (a), (b), except for the sensitivity tests.

method in the control run. The results indicate that cloud organization (Fig. 19), as well as stratiform rain percentage at the surface (Table 6), is affected for both the May and June cases. Clouds and cloud systems in the sensitivity tests are less organized compared to the control runs.

However, surface rainfall and the individual terms in the temperature and water vapor budgets change only slightly (less than 1%). Using the same horizontal winds at the surface in the sensitivity tests is the main reason for the small difference in the surface fluxes between the sensitivity tests and the control runs. The thermodynamic structure of the boundary layer does not change significantly as the same large-scale advective forcing in temperature and water vapor is applied to both the sensitivity tests and the control runs. The domain- and time-averaged hydrometeor contents do not change between the sensitivity tests and control runs (not shown). Consequently, the radiation and Q_1 and Q_2 budgets do not change in the sensitivity tests. Similar results were obtained for a three-dimensional model simulation (Tao and Soong 1986). However, this might not be the case in the real atmosphere, since the large-scale advective forcing might be effected significantly when there is no large-scale environmental wind shear. Other cloud-resolving model simulations without applying the large-scale forcing have shown that initial wind profiles can strongly influence the dynamics and rainfall predictions of model clouds (e.g., Cotton and Tripoli 1978; Wilhelmson and Klemp 1978; and many others).

6. Summary and conclusions

During SCSMEX (May–June 1998), two convectively active periods occurred over the northern South China Sea. The first active period (18–26 May) occurred shortly after the onset of the monsoon (15 May), while the second period (2–11 June) followed a week-long break in convection. The two-dimensional version of the GCE model has been used to simulate these two SCSMEX convective active periods. Observed large-scale advective tendencies (or forcing) of potential temperature, water vapor mixing ration, and horizontal momentum (Johnson and Ciesielski 2002) are used as the main forc-

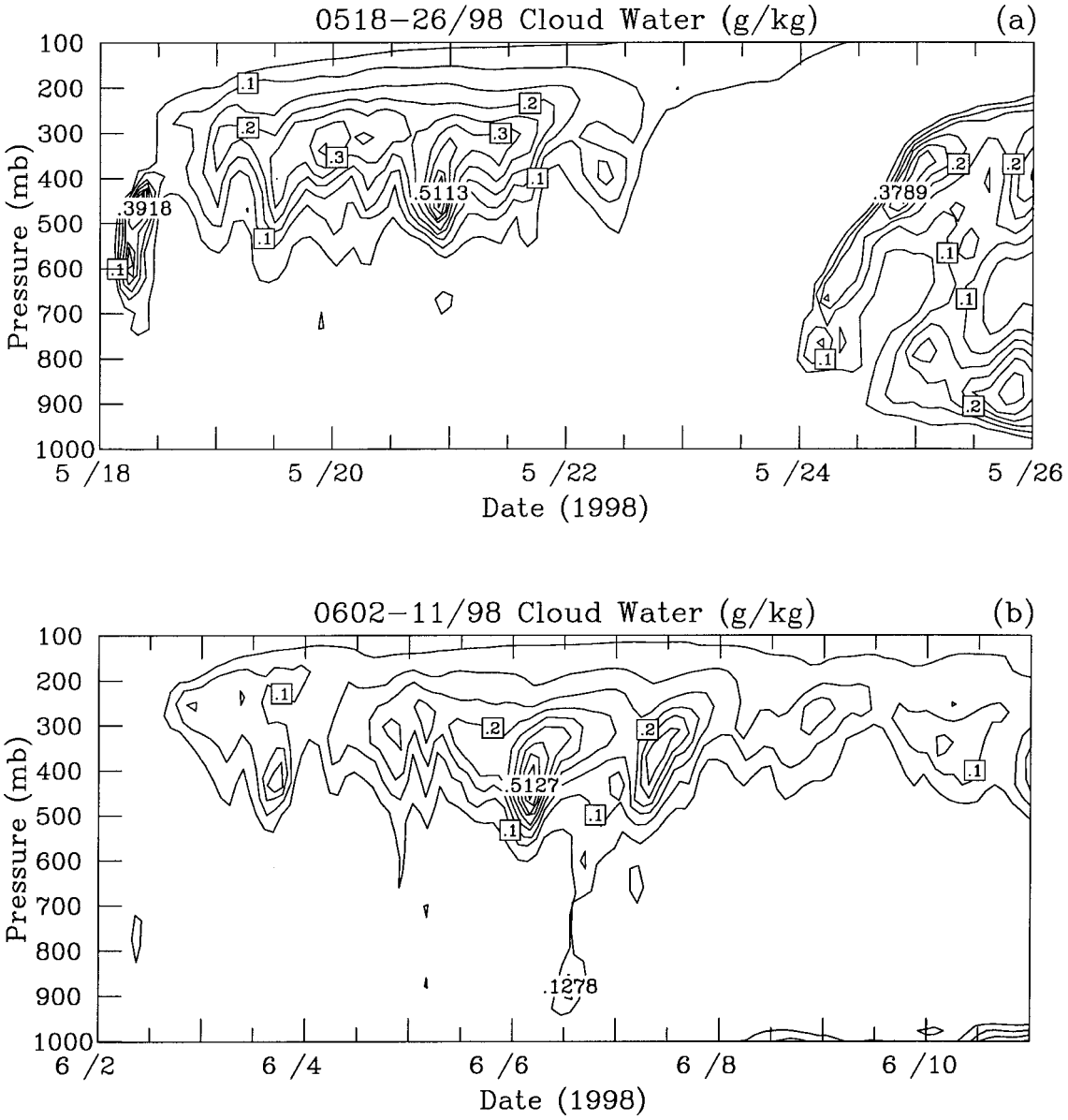

FIG. 17. (a) Evolution of the domain-averaged cloud water (g kg^{-1}) for the May SCSMEX case. (b) Same as (a), except for the Jun case.

ing in governing the GCE model in a semiprognostic manner (Soong and Tao 1980; Tao and Soong 1986; and many others). The June active period was characterized with stronger forcing in both the temperature and moisture fields, as well as larger low-level vertical wind shear in the *u*-wind component and greater CAPEs.

The major results can be summarized as follows.

- The GCE model results captured many of the observed precipitation characteristics. For example, the model-simulated rainfall temporal variation compared quite well to the sounding-estimated rainfall. However, the model underestimates the rainfall by 17% to 20% compared to that calculated based on soundings. The discrepancy in large-scale forcing in temperature and water vapor would cause differences between the the sounding-estimated and modeled rainfall (Tao et al. 2000). The GCE model-simulated rainfall for June is in very good agreement with the TRMM PR and GPCP, but not the TMI.
- Unicell (May case) and multicell (June case) types of convective systems are simulated by the model. They are determined by the observed mean *U* wind shear (unidirectional or reverse shear profiles above mid-level). Both types of convective systems can contribute large amounts of rainfall and associated latent heating.
- The time- and domain-averaged heating and moisture budgets are generally in good agreement with those

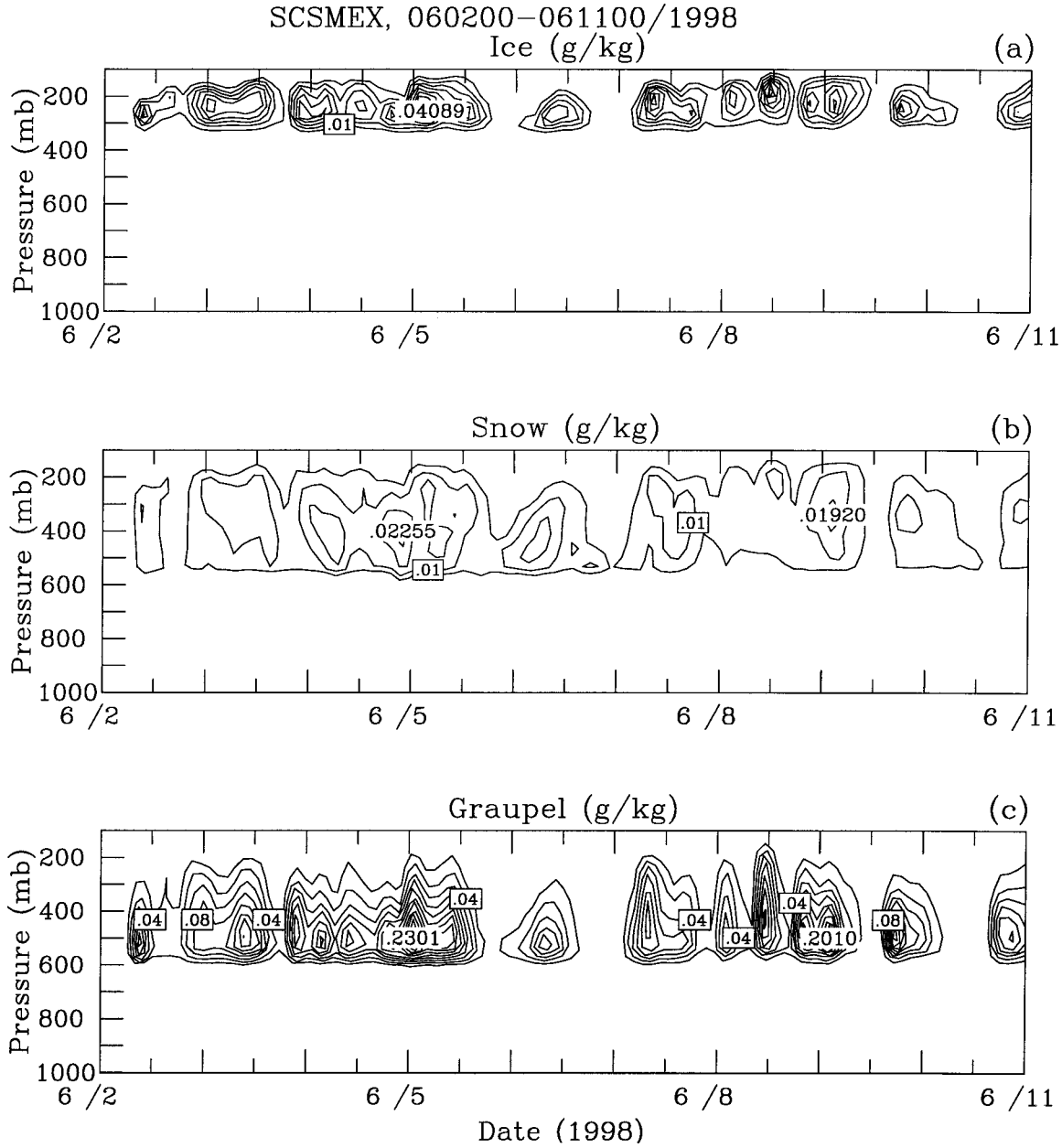

FIG. 18. Evolution of the domain-averaged (a) cloud ice, (b) snow, and (c) graupel for the 9-day period 2–11 Jun 1998. (d), (e), (f) Same as (a), (b), and (c), except for the microphysical sensitivity tests. The contour interval is 0.005, 0.005, and 0.02 g kg^{-1}, for (a), (b), and (c), respectively.

diagnostically determined from soundings. Overall, the model agrees better with observations in the June case than in the May case. The convective events are stronger in the June case, which may explain why it agrees better with observations.

- The contribution by eddy heat flux convergence/divergence in the Q_1 budget cannot be neglected at middle levels. This feature is related to localized cooling by the melting process. Net radiation results in cooling, and it contributes about 30% of the net condensation. The June case has larger net condensation because it has stronger large-scale advective forcing in temperature. This new finding is quite different from previous modeling studies.
- The net vertical eddy convergence/divergence of moisture by clouds is quite important for the Q_2 budget. The larger contribution by vertical eddy convergence/divergence in the Q_2 budget is the main reason for Q_1 and Q_2 decoupling. The typical convective and stratiform Q_1 and Q_2 structures discussed in Houze (1997) and Johnson (1984) are captured by the model for both cases.

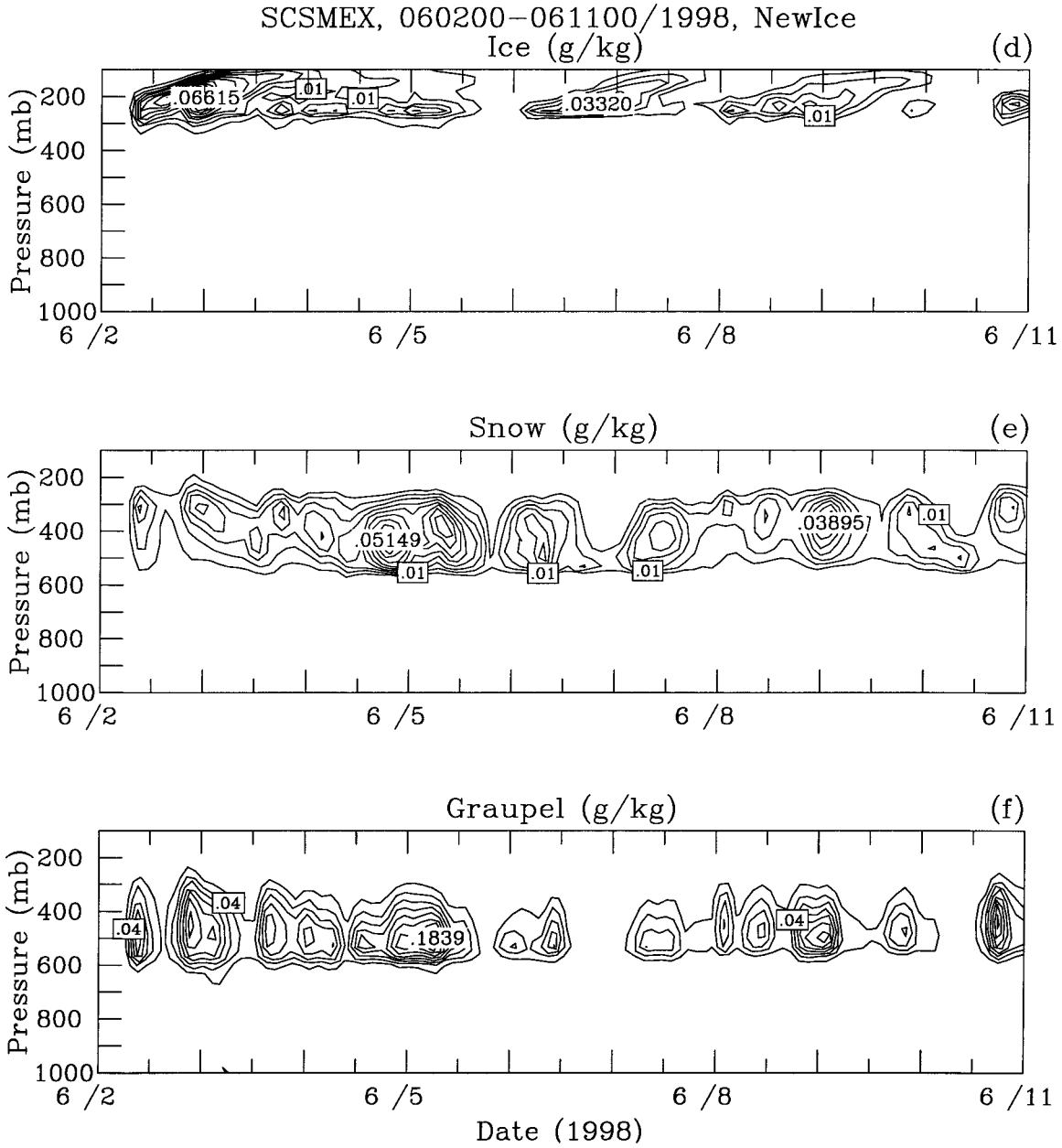

FIG. 18. (*Continued*)

- The energy budgets are calculated and results show that there are more latent heat fluxes prior to the onset of the monsoon (May case). The sensible heat fluxes do not contribute to precipitation processes in either SCSMEX case. Also, there is more large-scale advective forcing in water vapor (moistening) than temperature (cooling). This suggests that the imposed large-scale advective forcing in water vapor is very important for convective processes in the SCSMEX cases.
- Sensitivity tests are performed to examine the impact of the radiation, microphysics, and large-scale mean horizontal wind on the organization and intensity of the SCSMEX convective systems. Total rain production is reduced by about 17%–18% in the ice-free runs. The model results are also sensitive to ice processes and cloud-radiation interaction. The large-scale mean horizontal wind can play an important role in the organization of the cloud systems but not the precipitation processes. This is simply because the imposed large-scale advection in temperature and water vapor is the major forcing that determines the precipitation processes.

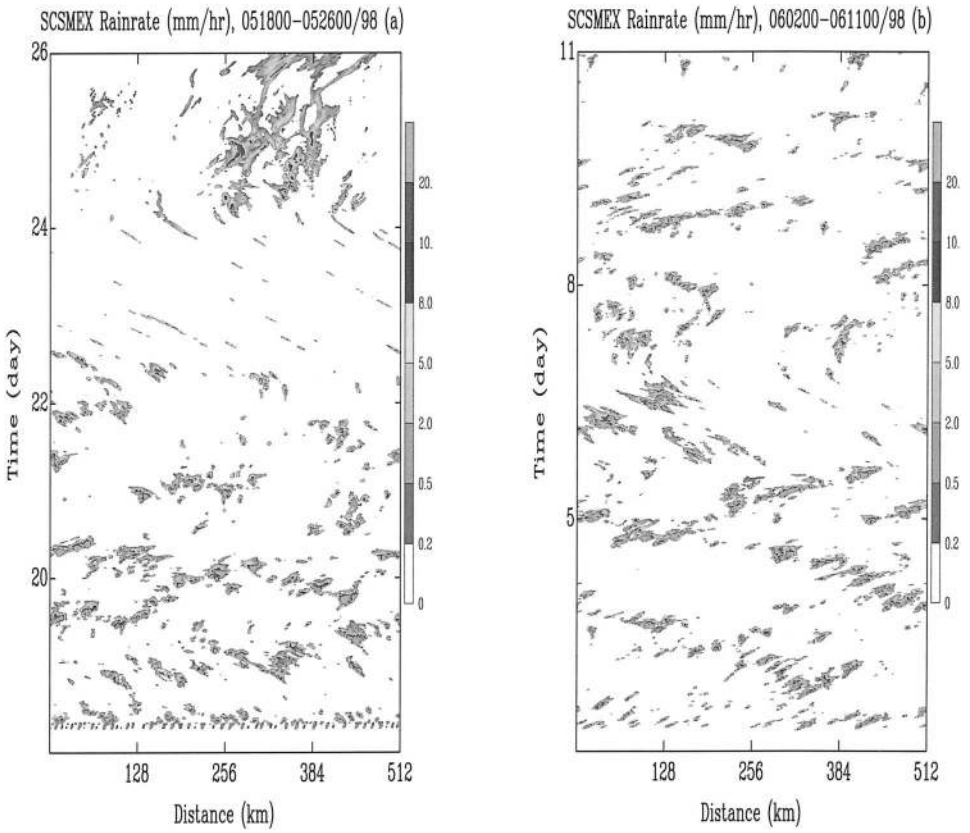

FIG. 19. Same as Fig. 5, except for the wind shear sensitivity tests.

Real clouds and cloud systems are three-dimensional. Few 3D CRMs (e.g., Tao and Soong 1986; Tao et al. 1987; Lipps and Hemler 1986) have been used to study the response of clouds to large-scale forcing. The 3D GCE modeling results, however, are in better agreement with the aircraft-measured updrafts and downdrafts (Zipser and LeMone 1980) in the middle troposphere. In these 3D simulations, the model domain was small and integration time was 6 h. Only recently, 3D experiments were performed for multiday periods for tropical cloud systems with large horizontal domains (Grabowski et al. 1998; Donner et al. 1999; Petch and Gray 2001; Xu et al. 2002; Tao 2003). Recently, an improved 3D GCE model was used to simulate periods during TOGA COARE and GATE and these two SCSMEX cases using a 512 km by 512 km domain (with 2-km resolution). The preliminary results indicate that cloud statistics, as well as surface precipitation and latent heating profiles, are very similar to the 2D GCE model simulations. Grabowski et al. (1998) also found a similar conclusion for their GATE and TOGA COARE multiday 2D and 3D simulations. Petch and Gray (2001) also showed that the surface rainfall between their 2D and 3D TOGA COARE simulations is within a few percent. The reason for the strong similarity between the 2D and 3D CRM simulations is that the same observed large-scale advective tendencies of temperature and water vapor mixing ratio were used as the main forcing in both the 2D and 3D models (Tao et al. 1987). However, the 3D GCE-modeled water vapor (Q_2) budget is usually in better agreement with observations in the lower troposphere than its 2D counterpart. Results from the 3D GCE model are in the process of being analyzed and will be reported in a publication in the near future.

Acknowledgments. This work is mainly supported by the NASA Headquarters Atmospheric Dynamics and Thermodynamics Program and the NASA Tropical Rainfall Measuring Mission. The authors are grateful to Dr. R. Kakar at NASA headquarters for his support of this research. Dr. R. H. Johnson and Dr. P. E. Ciesielski are supported by NASA/TRMM NAG5-9665. The authors thank two anonymous reviewers for their constructive comments. The authors also thank Mr. S. Lang for reading the manuscript.

Acknowledgment is also made to the NASA Goddard Space Flight Center for computer time used in this research.

REFERENCES

Caniaux, G., J.-L. Redelsperger, and J.-P. Lafore, 1994: A numerical study of the stratiform region of a fast-moving squall line. Part

I: General description and water and heat budgets. *J. Atmos. Sci.,* **51,** 2046–2074.
Chin, H.-N. S., 1994: The impact of the ice phase and radiation on a midlatitude squall line system. *J. Atmos. Sci.,* **51,** 3320–3343.
——, Q. Fu, M. M. Bradley, and C. R. Molenkamp, 1995: Modeling of a tropical squall line in two dimensions and its sensitivity to environmental winds and radiation. *J. Atmos. Sci.,* **52,** 3172–3193.
Chong, M., and D. Hauser, 1990: A tropical squall line observed during the COPT 81 experiment in West Africa. Part III: Heat and moisture budgets. *Mon. Wea. Rev.,* **118,** 1696–1706.
Churchill, D. D., and R. A. Houze Jr., 1984: Development and structure of winter monsoon cloud clusters on 10 December 1978. *J. Atmos. Sci.,* **41,** 933–960.
Cotton, W. R., and G. J. Tripoli, 1978: Cumulus convection in shear flow—Three-dimensional numerical experiments. *J. Atmos. Sci.,* **35,** 1053–1521.
Donner, L. J., C. J. Seman, and R. S. Hemler, 1999: Three-dimensional cloud-system modeling of GATE convection. *J. Atmos. Sci.,* **56,** 1885–1912.
Dudhia, J., M. W. Moncrieff, and D. W. K. So, 1987: The two-dimensional dynamics of West African squall lines. *Quart. J. Roy. Meteor. Soc.,* **113,** 121–146.
Fairall, C., E. F. Bradley, D. P. Rogers, J. B. Edson, and G. S. Young, 1996: Bulk parameterization of air–sea fluxes for TOGA COARE. *J. Geophy. Res.,* **101,** 3747–3764.
Fovell, R. G., and Y. Ogura, 1988: Numerical simulation of a midlatitude squall line in two dimensions. *J. Atmos. Sci.,* **45,** 3846–3879.
Fu, Q., S. K. Krueger, and K. N. Liou, 1995: Interactions of radiation and convection in simulated tropical cloud clusters. *J. Atmos. Sci.,* **52,** 1310–1328.
Grabowski, W. W., X. Wu, M. W. Moncrieff, and W. D. Hall, 1998: Cloud-resolving modeling of cloud systems during Phase III of GATE. Part II: Effects of resolution and the third spatial dimension. *J. Atmos. Sci.,* **55,** 3264–3282.
Houze, R. A., Jr., 1977: Structure and dynamics of a tropical squall-line system. *Mon. Wea. Rev.,* **105,** 1540–1567.
——, 1982: Cloud clusters and large-scale vertical motions in the Tropics. *J. Meteor. Soc. Japan,* **60,** 396–409.
——, 1997: Stratiform precipitation in regions of convection: A meteorological paradox. *Bull. Amer. Meteor. Soc.,* **78,** 2179–2196.
Johnson, D., W.-K. Tao, J. Simpson, and C.-H. Sui, 2002: A study of the response of deep tropical clouds to large-scale processes, Part I: Model setup strategy and comparison with observation. *J. Atmos. Sci.,* **59,** 3492–3518.
Johnson, R. H., 1984: Partitioning tropical heat and moisture budgets into cumulus and mesoscale components: Implication for cumulus parameterization. *Mon. Wea. Rev.,* **112,** 1590–1601.
——, and P. E. Ciesielski, 2002: Characteristics of the 1998 summer monsoon onset over the northern South China Sea. *J. Meteor. Soc. Japan,* **80,** 561–578.
Klemp, J. B., and R. Wilhelmson, 1978: The simulation of three-dimensional convective storm dynamics. *J. Atmos. Sci.,* **35,** 1070–1096.
Krueger, S. K., 1988: Numerical simulation of tropical cumulus clouds and their interaction with the subcloud layer. *J. Atmos. Sci.,* **45,** 2221–2250.
Lang, S., W.-K. Tao, J. Simpson, and B. Ferrier, 2003: Numerical modeling of convective–stratiform precipitation processes: Sensitivity to partition methods. *J. Appl. Meteor.,* **42,** 505–527.
Lau, K. M., and Coauthors, 2000: A report of the field operations and early results of the South China Sea Monsoon experiment (SCSMEX). *Bull. Amer. Meteor. Soc.,* **81,** 1261–1270.
Lin, Y.-L., R. D. Farley, and H. D. Orville, 1983: Bulk parameterization of the snow field in a cloud model. *J. Climate Appl. Meteor.,* **22,** 1065–1092.
Lipps, F. B., and R. S. Hemler, 1986: Numerical simulation of deep tropical convection associated with large-scale convergence. *J. Atmos. Sci.,* **43,** 1796–1816.
McCumber, M., W.-K. Tao, J. Simpson, R. Penc, and S.-T. Soong, 1991: Comparison of ice-phase microphysical parameterization schemes using numerical simulations of convection. *J. Appl. Meteor.,* **30,** 985–1004.
Miller, R. A., and W. M. Frank, 1993: Radiative forcing of simulated tropical cloud clusters. *Mon. Wea. Rev.,* **121,** 482–498.
Moncrieff, M. W., S. K. Krueger, D. Gregory, J.-L. Redelsperger, and W.-K. Tao, 1997: GEWEX Cloud System Study (GCSS) Working Group 4: Precipitating convective cloud systems. *Bull. Amer. Meteor. Soc.,* **78,** 831–845.
Petch, J. C., and M. E. B. Gray, 2001: Sensitivity studies using a cloud-resolving model simulation of the tropical west Pacific. *Quart. J. Roy. Meteor. Soc.,* **127,** 2287–2306.
Redelsperger, J. L., and Coauthors, 2000: A GCSS model intercomparison for a tropical squall line observed during TOGA-COARE. Part 1: Cloud-resolving models. *Quart. J. Roy. Meteor. Soc.,* **126,** 823–864.
Rutledge, S. A., and P. V. Hobbs, 1984: The mesoscale and microscale structure and organization of clouds and precipitation in midlatitude clouds. Part XII: A diagnostic modeling study of precipitation development in narrow cold frontal rainbands. *J. Atmos. Sci.,* **41,** 2949–2972.
Simpson, J., N. Westcott, R. Clerman, and R. A. Pielke, 1980: On cumulus mergers. *Arch. Meteor. Geophys. Bioklim.,* **29A,** 1–40.
——, R. F. Adler, and G. R. North, 1988: A proposed satellite tropical rainfall measuring mission (TRMM). *Bull. Amer. Meteor. Soc.,* **69,** 278–295.
——, C. Kummerow, W.-K. Tao, and R. Adler, 1996: On the Tropical Rainfall Measuring Mission (TRMM). *Meteor. Atmos. Phys.,* **60,** 19–36.
Smolarkiewicz, P. K., and W. W. Grabowski, 1990: The multidimensional positive advection transport algorithm: Nonoscillatory option. *J. Comput. Phys.,* **86,** 355–375.
Soong, S.-T., and Y. Ogura, 1980: Response of tradewind cumuli to large-scale processes. *J. Atmos. Sci.,* **37,** 2035–2050.
——, and W.-K. Tao, 1980: Response of deep tropical clouds to mesoscale processes. *J. Atmos. Sci.,* **37,** 2016–2036.
Steiner, M. R., R. A. Houze Jr., and S. E. Yuter, 1995: Climatological characterization of three-dimensional storm structure from operational radar and rain gauge data. *J. Appl. Meteor.,* **34,** 1978–2007.
Sui, C. H., K.-M. Lau, and X. Li, 1998: Convective–radiative interaction in simulated diurnal variations of tropical cumulus ensemble. *J. Atmos. Sci.,* **55,** 2345–2357.
Tao, W.-K., 2003: Goddard Cumulus Ensemble (GCE) model: Application for understanding precipitation processes. *Cloud Systems, Hurricanes, and the Tropical Rainfall Measurement Mission (TRMM): A Tribute to Dr. Joanne Simpson, Meteor. Monogr.,* No. 51, Amer. Meteor. Soc., 103–138.
——, and J. Simpson, 1984: Cloud interactions and merging: Numerical simulations. *J. Atmos. Sci.,* **41,** 2901–2917.
——, and S.-T. Soong, 1986: A study of the response of deep tropical clouds to mesoscale processes: Three-dimensional numerical experiments. *J. Atmos. Sci.,* **43,** 2653–2676.
——, and J. Simpson, 1989: Modeling study of a tropical squall-type convective line. *J. Atmos. Sci.,* **46,** 177–202.
——, and ——, 1993: The Goddard Cumulus Ensemble Model. Part I: Model description. *Terr. Atmos. Oceanic Sci.,* **4,** 19–54.
——, ——, and S.-T. Soong, 1987: Statistical properties of a cloud ensemble: A numerical study. *J. Atmos. Sci.,* **44,** 3175–3187.
——, J. Simpson, C.-H. Sui, B. Ferrier, S. Lang, J. Scala, M.-D. Chou, and K. Pickering, 1993: Heating, moisture and water budgets of tropical and midlatitude squall lines: Comparisons and sensitivity to longwave radiation. *J. Atmos. Sci.,* **50,** 673–690.
——, J. Scala, B. Ferrier, and J. Simpson, 1995: The effects of melting processes on the development of a tropical and a midlatitude squall line. *J. Atmos. Sci.,* **52,** 1934–1948.
——, J. Simpson, S. Lang, C.-H. Sui, B. Ferrier, and M.-D. Chou, 1996: Mechanisms of cloud–radiation interaction in the Tropics and midlatitudes. *J. Atmos. Sci.,* **53,** 2624–2651.

——, S. Lang, J. Simpson, W. S. Olson, D. Johnson, B. Ferrier, C. Kummerow, and R. Adler, 2000: Vertical profiles of latent heat release and their retrieval in TOGA COARE convective systems using a cloud resolving model, SSM/I and radar data. *J. Meteor. Soc. Japan*, **78,** 333–355.

——, and Coauthors, 2003: Microphysics, radiation and surface processes in a non-hydrostatic model. *Meteor. Atmos. Phys.,* **82,** 97–137.

Wang, Y., W.-K. Tao, and J. Simpson, 1996: The impact of ocean surface fluxes on a TOGA COARE cloud system. *Mon. Wea. Rev.,* **124,** 2753–2763.

Wilhelmson, R. B., and J. B. Klemp, 1978: A numerical study of storm splitting that leads to long-lived storms. *J. Atmos. Sci.,* **35,** 1975–1986.

Wu, X., W. W. Grabowski, and M. W. Moncrieff, 1998: Long-term behavior of cloud systems in TOGA COARE and their interactions with radiative and surface processes. Part I: Two-dimensional modeling study. *J. Atmos. Sci.,* **55,** 2693–2714.

Xu, K.-M., 1995: Partitioning mass, heat, and moisture budgets of explicit simulated cumulus ensembles into convective and stratiform components. *J. Atmos. Sci.,* **52,** 551–573.

——, and D. A. Randall, 1995: Impact of interactive radiative transfer on the microscopic behavior of cumulus ensembles. Part II: Mechanisms for cloud–radiation interactions. *J. Atmos. Sci.,* **52,** 800–817.

——, and ——, 1996: A semiemprical cloudiness parameterization for use in climate models. *J. Atmos. Sci.,* **53,** 3084–3102.

——, and Coauthors, 2002: Intercomparison of cloud-resolving models with the ARM Summer 1997 IOP data. *Quart. J. Roy. Meteor. Soc.,* **128,** 593–624.

Yanai, M., S. Esbensen, and J. Chu, 1973: Determination of average bulk properties of tropical cloud clusters from large-scale heat and moisture budgets. *J. Atmos. Sci.,* **30,** 611–627.

Zipser, E. J., 1977: Mesoscale and convective-scale downdrafts as distinct components of squall-line structure. *Mon. Wea. Rev.,* **105,** 1568–1589.

——, and M. A. LeMone, 1980: Cumulonimbus vertical velocity events in GATE. Part II: Synthesis and model core structure. *J. Atmos. Sci.,* **37,** 2458–2469.